Paper I

Observations of turbulent mixing and hydrography in the marginal ice zone of the Barents Sea

Arild Sundfjord[1,2], Ilker Fer[3,1], Yoshie Kasajima[3,1] and Harald Svendsen[1]

[1] Geophysical Institute, University of Bergen, Bergen,

[2] Norwegian Polar Institute, Tromsø

[3] Bjerknes Centre for Climate Research, Bergen

Accepted for publication in Journal of Geophysical Research.

Abstract

Measurements of hydrography, currents, microstructure shear and temperature were made at ice drift stations in the marginal ice zone (MIZ) of the northern Barents Sea. Highly variable mixing regimes were observed within and below the pycnocline. Elevated turbulent dissipation (5-15×10^{-7} W kg^{-1}) was associated with strong vertical shear between the surface layer and the sub-surface currents, as well as strong tidal flow over shallow topography. Dissipation in the pycnocline was enhanced at stations with strong wind forcing. During drifts under relatively calm wind and away from strong fronts and abrupt topography, station-mean dissipation was up to a factor 50 lower and double diffusive convection contributed significantly to the vertical heat flux where hydrography favored diffusive layering. Independent measures of turbulent length scale from density overturns compared well with those inferred from the dissipation measurements. The variability of dissipation was better captured using a scaling by shear suggested for shelves, in contrast to by shear variance suggested for the deep open ocean. Sufficiently resolved patches of enhanced temperature microstructure used in combination with dissipation measurements suggest mixing efficiency comparable to the conventional upper bound of R_f~0.17. Water mass modification and fluxes of nutrients and dissolved carbon were observed to have large local variability in accordance with the observed variability of vertical mixing in the MIZ.

Keywords

Turbulence, mixing, dissipation, marginal ice zone, Barents Sea

1 Introduction

This work is part of an integrated physical-biological-chemical project, “Carbon flux and ecosystem feed back in the northern Barents Sea in an era of climate change” (CABANERA), aimed at assessing how the extent and position of the marginal ice zone (MIZ) influence the natural and anthropogenic carbon cycle. The efficiency of vertical mixing and diffusion processes controls the vertical exchanges of the carbon system constituents, thus influencing how CO_2 is absorbed by the ocean from the atmosphere, dissolved, and further transported deeper in the water column. Detailed knowledge of the mixing processes is necessary to quantify the rate at which nutrients become available to primary production and thus increase the biological uptake of carbon in the surface layer. The Barents Sea may act to mitigate the increase in the atmospheric CO_2 content. In this large transit shelf sea, water properties are substantially modified [*Pfirman et al.*, 1994]. Atlantic water entering the Barents Sea from the south loses heat, thus enhancing its ability to absorb CO_2 from the atmosphere [*Kaltin et al.*, 2002]. Recent studies suggest that large amounts of CO_2 from the atmosphere can be sequestered through surface cooling and brine rejection during ice freezing [*Omar et al.*, 2003]. Primary production is comparatively large in the Barents Sea [*Sakshaug*, 2004], which is crucial for the transformation of carbon from inorganic to organic form and possible burial in sediments.

The MIZ of the Barents Sea is considered to be important both for water mass modification and biological production, yet studies of the oceanic turbulence are relatively scarce in this environment. Results and insight gained from previous turbulence studies at other sites are not directly applicable because e.g. previous drift measurements under sea ice were typically from thick drifting pack-ice [*Padman and Dillon*, 1991; *Robertson et al.*, 1995; *McPhee and Stanton*, 1996] or from fast-ice [*Crawford et al.*, 1999], under which the effects of wind and ocean currents will be different than in the upper part of the water column of a shelf sea MIZ. Experiments using mast-mounted instruments at fixed depths and focusing primarily on the under-ice boundary layer have been performed e.g. in the Greenland Sea MIZ [*Morison et al.*, 1987]. Vertical profiling studies on ice-free shelves [e.g. *MacKinnon and Gregg*, 2003b; *Fer*, 2006], and near shelf breaks [*Inall et al.*, 2000], will have relevance for the processes in the Barents Sea, but again the turbulence characteristics in the upper part of the water column will be different.

The purpose of this paper is to describe the vertical mixing processes in the Barents Sea MIZ, and to relate the mixing within and below the pycnocline to hydrography, currents, wind and tides and discuss consequences for water mass transformations and the biogeochemical cycles. A better understanding of these relations will help to improve their representation in numerical ocean models, including those incorporating biogeochemical cycles.

The data set presented herein was collected from the *R.V. Jan Mayen* during two multi-disciplinary cruises as a joint effort of the CABANERA and the Polar Ocean Climate Processes (ProClim) projects. A detailed account of the upper ocean boundary layer dynamics is given in *Fer and Sundfjord* [2006].

The study area and the dominant water masses and current systems are described in section 2. In section 3, an overview of the sampling and instrumentation is given, along with data processing routines and methods for quantification of turbulent dissipation and diffusivity. The characteristics of hydrography and currents, and observations of turbulent dissipation and mixing are presented in section 4. Subsequently in section 5, we compare turbulence measurements with available methods and parameterizations and relate observations to forcing mechanisms and hydrography. A discussion of implications for water mass modification, nutrient fluxes and carbon cycling is given in section 6, followed by a summary in section 7.

2 Survey site and water masses

The Barents Sea is a shelf sea with a complex bottom topography with depths ranging from 50 m at the shallow banks to 500 m in the deeper channels and troughs (average depth ~230 m), and is an area of confluence and mixing of different water masses. Warm, saline and nutrient-rich Atlantic Water (AW, $T>3°C$, $S>34.95$ as defined by *Carmack* [1990]) enters the Barents Sea from the south-west, between Norway and Bear Island. Away from the coast, AW occupies the whole water column in the southern part of the Barents Sea. After crossing the Polar Front, the AW subducts to a core depth of ~150-250 m [*Loeng*, 1991], beneath relatively cold and less-saline water, and it can be found in most of the central and north-eastern Barents Sea in modified form. The AW throughflow in the Barents Sea exits between Novaya Zemlya and Franz Josef Land (typically with $T<0°C$ [*Schauer et al.*, 2002a]) and then continues north-east to the shelf break at St. Anna Trough (see Figure 1 for place names). The Barents Sea branch of AW contributes to the lower part of the cold halocline – the transitional layer isolating the cold upper surface waters from the warmer water of Atlantic origin below - and to the renewal of intermediate water in the Arctic Ocean [*Schauer et al.*, 2002b].

A northern AW current branch, the West Spitsbergen Current (WSC), follows the west coast of Spitsbergen and the continental slope eastwards into the Arctic Ocean [*Mosby*, 1938] where it submerges below less-saline water. Along the northern perimeter of the Barents Sea, WSC has its core at ~100-150 m [*Saloranta and Haugan*, 2001]. The volume fluxes of the WSC and the Barents Sea branch of AW are comparable [*Schauer et al.*, 2002b], but the WSC retains more of the AW characteristics and is swifter. The bulk of the heat supplied to the interior Arctic Ocean is therefore contained in the WSC. This northern AW branch also contributes to the halocline and intermediate waters of the deep Arctic Ocean, in particular of the Nansen and Amundsen basins. Part of this current flows into the northern Barents Sea through deep channels around Franz Josef Land and Kvitøya [*Pfirman et al.*, 1994].

Ice and low-salinity surface water enters the northern Barents Sea mainly from the interior Arctic Ocean and the Kara Sea. Following *Pfirman et al.* [1994], we define Arctic Water (ArW) with $34.3<S<34.7$ and $T<-1$°C. A seasonal Surface Melt Water (SMW, with S typically less than that of ArW) forms during summer.

The tidal currents in the northern and western Barents Sea are among the strongest found on the Arctic Ocean shelves [*Kowalik and Proshutinsky*, 1994], particularly around Bear

Island and Spitsbergen Bank [*Kowalik and Proshutinsky*, 1995]. Other sub-surface net currents, in addition to the AW flows, are density driven [*Aadlandsvik and Loeng*, 1991].

The wind regime of the Barents Sea is dominated by the passage of low pressure systems, typically from southwest to northeast, correlated with the strength of the low pressure near Iceland. Winds are particularly strong in winter with frequent gale-force storms [*Gathman*, 1986], mainly due to the annual cycle of the Icelandic low. The local wind stress is generally larger away from the ice edge compared to the interior pack-ice, due to the corresponding differences in air-sea exchanges [*Guest et al.*, 1995].

3 Measurements and methods

3.1 Survey overview

During two cruises, 20 July-03 August 2004 and 18 May-04 June 2005, measurements of currents, hydrography and microscale shear, temperature, and conductivity were made at eight drift stations in the northern Barents Sea and across the shelf break into the deep Arctic Ocean (Figure 1). Measurements were occasionally interrupted due to ice and weather conditions or instrument malfunction. Observations of hydrography and currents are given for all stations, whereas turbulence characteristics are presented for the six stations with the most comprehensive data sets. A survey overview is given in Table 1. Time is given as decimal day of year (doy), with doy=0.5 at 12:00 UTC on 1 January.

At all stations, except the open water station XVIII, the *R.V. Jan Mayen* stayed moored or close to a selected large ice floe. Occasionally the vessel deviated from the drift to perform diverse operations in the vicinity or to adjust her heading to the prevailing wind direction.

3.2 Wind, ice, and tides

Wind speed and direction at 10-m height were recorded at 1 minute intervals by an automatic ship-mounted weather station and were corrected for the ship speed logged from a GPS system. After removing spikes induced by abrupt vessel motion, wind stress was calculated from $\tau = \rho_{air} C_D W^2$ where $\rho_{air} = 1.25$ kg m^{-3} is the density of air, C_D is the air-ice-sea drag coefficient and W is the wind speed. We use $C_D = 2.7\times10^{-3}$ based on the threshold values between the 50 % ice-covered outer and diffuse MIZ regions [*Guest et al.,* 1995]. The work done by the wind is $E_{10} = \tau W = \rho_{air} C_D W^3$.

The ice cover was visually assessed from the vessel at 10 % cover classes. Average ice thickness and floe keel depth were measured by scuba divers using pressure gauges along transects below the main ice floe near which the sampling was done. The ice parameters given in Table 1 are representative of the stations but some local variability is expected.

The current measurements (section 3.3) do not resolve the whole water column and are not of sufficient duration to reliably infer tidal constituents. We therefore compute tidal elevations and currents for the study area using the high-resolution Arctic Ocean Tidal Inverse Model (AOTIM) and the OSU Tidal Inversion Software (OTIS). In addition to harmonic constants, elevation and velocity data based on satellite altimetry (Topex/Poseidon and ERS), AOTIM (http://www.coas.oregonstate.edu/research/po/research/tide/Arc.html) also comprises tidal gauge data assimilation [*Padman and Erofeeva*, 2004, and references therein]. A least-squares fit is used for modelling the shallow water tidal equations, with data interpolated from a 5 km resolution grid.

3.3 Current measurements

Ocean current profiles were collected using a vessel-mounted 150 kHz RD Instruments Acoustic Doppler Current Profiler (ADCP). Continuous profiles were averaged every 5 min in 8 m (2004) and 4 m (2005) depth bins with the first bin centered at ~21 m and 15 m, respectively, and the deepest bin with good data at ~250 m. Absolute currents were obtained by referencing to the surface, and were found to be in good agreement with bottom track referencing when available.

The magnitude of shear, $Sh = ((\partial u/\partial z)^2 + (\partial v/\partial z)^2)^{1/2}$, where u and v are the east and north components of the velocity, was computed by first differencing at 16-m moving intervals. Accordingly, the first value of shear is at 29 m (2004) and 23 m (2005). The 16-m interval was chosen to avoid the contribution of noise which increasingly dominated the vertical wavenumber spectra at increasing wavenumbers (decreasing length scale).

3.4 Hydrography

Conductivity, temperature, depth (CTD) profiles were made using a Sea-Bird SBE9 system. During part of the 2004 cruise this instrument malfunctioned and a SAIV SD204 CTD system with relatively crude resolution and accuracy was deployed. The SBE9 was calibrated post-cruise in 2004, and the data corrected for drift were used to calibrate the SAIV data. In 2005, CTD data were calibrated against salinity samples analysed with a Guildline Portasal Salinometer at the Geophysical Institute, University of Bergen. All corrected CTD data were post-processed according to standard procedures as recommended by the manufacturer, and bin averaged to 1 m resolution. Precision temperature and conductivity measurements at higher resolution were made with the microstructure profiler described in the following section.

The depth of the surface mixed layer (D_{mixed}) was calculated using the Split-and-Merge method decribed by *Thomson and Fine* [2003]. We used an improved version (kindly provided by R. Thomson) which includes a second run through the split-and-merge procedure using a lower boundary depth determined by the first run. The sensitivity of the results to initial choices of boundary depth, error threshold (here, set to 0.5 and 0.05 for the first and the second run, respectively), and number of segment breakup points is thus reduced.

The base of the pycnocline (D_{pyc}) was identified objectively as the first depth below the depth of maximum density gradient where the density difference was less than 0.01 kg m^{-3} per meter for at least three consecutive 1-m intervals.

3.5 Turbulence and mixing

MSS profiler, deployment and data reduction

At the six selected stations (Table 2), a total of 155 microstructure profiles in 43 sets were collected using a 1.4 m long loosely-tethered free-fall MSS profiler [*Prandke and Stips*, 1998]. The instrument is equipped with two airfoil shear probes (PNS98) aligned parallel to each other, fast response conductivity (capillary type two electrode probe) and temperature (FP07) sensors, an acceleration sensor, and conventional CTD sensors for precision measurements. All sensors sample at 1024 Hz to 16 bit resolution. The sensors are protected by a probe guard which is the source of two significant narrow-band noise peaks in the shear spectra at ~24 Hz and at 44 Hz. The buoyancy of the instrument is adjusted to a typical fall speed of 0.7-0.9 m s^{-1}. With a nominal fall speed of 0.8 m s^{-1}, the 24 Hz peak induced by the guard corresponds to a wavenumber of 30 cycles per meter (cpm). The wavenumber range chosen for the analysis is well below this peak.

Several successive profiles, typically 3-5 repeats (hereinafter called a ‘set’), were conducted every ~4 h to cover different phases of the tidal cycle within the station time (20-43 h); a compromise in order to accommodate the multi-disciplinary user groups on the vessel. Occasionally turbulence profiles were interrupted by strong wind or rapid vessel/ice drift. A deployment overview is given in Table 1. The profiles were terminated at ~60 m in 2004 and at ~150 m in 2005. The dissipation in the upper 5-10 m have been discarded because of noise from instrument acceleration and turbulence generated by the ship’s keel.

Full-scan data acquired by all sensors are edited for transmission errors and spikes and then averaged to 256 Hz to reduce noise. Precision CTD data are low-passed at 10 Hz using a phase-preserving 4th order Butterworth filter. Temperature is then corrected for the time-response lag relative to the conductivity sensor using a 55 scan (for 256 Hz data) recursive filter. The profiles are averaged at 10 cm intervals (within ±0.05 dbar of 0.1 dbar interval target pressures, referred to as depth with negligible error). Conductivity is corrected against SBE deployed typically within 15-20 min of the MSS. Salinity is 0.5 m median-filtered to further reduce spikes prior to calculating potential temperature, θ, and potential density anomaly, σ_θ.

Stability and Richardson number

The buoyancy frequency, $N=[-(g/\rho)\,(\partial\sigma_\theta/\partial z)]^{1/2}$, is calculated using the Thorpe ordered σ_θ profiles [*Thorpe*, 1977] with density gradient obtained from the slope of linear fits of σ_θ against depth in 4-m sliding boxcar windows. The Richardson number, $Ri=N^2/Sh^2$, is calculated at moving 16-m intervals, below which the noise in the ADCP derived shear substantially increases. In Ri calculations, the buoyancy frequency is averaged at depth intervals corresponding with the depth range used to calculate shear. An average Ri profile is calculated for each MSS set using set averaged N^2 and Sh^2 averaged over 6 subsequent ADCP profiles (30 min) centered at the mean time of the MSS set.

Dissipation and eddy diffusivity

Time series of small-scale shear, $\partial u'/\partial z$, measured by the shear probes are converted into vertical wavenumber space using a smooth fall-speed profile, invoking Taylor's frozen turbulence hypothesis which is valid at the fall speeds reported here. The fall speed is derived from the time derivative of the 2-Hz low passed pressure record. The dissipation rate of turbulent kinetic energy per unit mass, ε, is calculated using the isotropic relation $\varepsilon = 7.5\nu\left\langle(\partial u'/\partial z)^2\right\rangle$ [*Yamazaki and Osborn*, 1990], where ν is the viscosity of seawater and $\partial u'/\partial z$ is the shear resolved at cm-scales. Here, ν is approximated as a function of temperature and ranges within $1.55\text{-}1.9\times10^{-6}$ m^2 s^{-1} for the recorded range of temperatures,

-1.8 to 5°C. Shear wavenumber spectra are calculated using half overlapping 256-point (1 s) Hanning windows, corresponding to 0.8-m for a nominal fall speed of 0.8 m s^{-1}. The shear variance is obtained by integrating the shear wavenumber spectrum between 2 cpm, a limitation due to the length of the profiler, and an upper cutoff number depending on the Kolmogorov wavenumber, $(\varepsilon/\nu^3)^{1/4}/2\pi$ cpm. The upper cutoff is determined by iteration, similar to that described in [*Moum et al.*, 1995], and is set to maximum 30 cpm (or 14 cpm when 2-14 cpm integrated $\varepsilon < 2 \times 10^{-8}$ W kg^{-1}). This range is not affected by the narrowband noise peaks (see e.g. the shear spectra in Figure 11, introduced later). A correction, typically within a factor of 1.2 for $\varepsilon < 10^{-7}$ W kg^{-1} and about a factor of 1.7 for $\varepsilon \sim 10^{-6}$ W kg^{-1}, is applied for the lost variance assuming the Nasmyth's form as tabulated in *Oakey* [1982]. A further check is employed by comparing dissipation values from both probes, and anomalous data were discarded prior to averaging at 0.5 m bins. The noise level measured in quiet regions appears to be about 1×10^{-8} W kg^{-1}, relatively high as a result of high fall speed and small mass of the profiler. "Pseudo" dissipation rates, derived identically from spectral analysis of the acceleration sensor divided by the fall speed [*Moum and Lueck*, 1985] are $< 10^{-10}$ W kg^{-1}.

The vertical diffusivity for mass is approximated using $K_\rho = \Gamma\varepsilon/N^2$ [*Osborn*, 1980], where Γ, the dissipation ratio, is related to the mixing efficiency. A commonly used value of Γ = 0.2 [*Moum*, 1996] yields an upper limit for K_ρ. When calculating K_ρ we adopt Γ=0.12 as recommended by *Arneborg* [2002] and consistent with the observations of *St Laurent and Schmitt* [1999]. A more detailed discussion is given in section 5.2.

An independent estimate of eddy diffusivity for heat, K_T, is made using the Osborn-Cox model [*Osborn and Cox*, 1972] as $K_T = 3k_TCx$, where $k_T = 1.4\times10^{-7}$ m^2 s^{-1} is the molecular diffusivity for heat, $Cx = \left\langle (\partial T'/\partial z)^2 \right\rangle / \left\langle \partial T/\partial z \right\rangle^2$ is the Cox number and the factor 3 assumes full isotropy. The dissipation of thermal variance is $\chi = 2k_T \left\langle 3(\partial T'/\partial z)^2 \right\rangle$. The temperature gradient spectrum in the dissipation range often adheres to the Batchelor form [*Dillon and Caldwell*, 1980]. Slow fall speed and a fast response temperature sensor with a known response function are needed to sufficiently resolve the temperature gradient spectrum. Because the signal acquired by the fast response temperature sensor was pre-emphasized for frequencies > 1 Hz in a separate channel, we were able to partly resolve the temperature gradient spectrum for active patches (in contrast to the resolved shear spectrum every 0.5 m). Thermal gradients are deconvolved from the pre-emphasized signal, and temperature spectra are obtained using the ideal transfer function for the ideal amplification of the circuit. The transfer function $H^2(f) = [1 + (2\pi f\tau W^{-0.32})^2]^{-2}$ [*Gregg and Meagher*, 1980] is applied to correct for the response time of the FP07. Here W is the fall rate of the profiler, f is the frequency in Hz and $\tau = 12\times10^{-3}$ s is the response time. We then convert this corrected temperature spectrum to $\partial T'/\partial t$ spectrum by multiplying by $(2\pi f)^2$. The frequency domain $\partial T'/\partial t$ spectrum is then converted to vertical wavenumber domain $\partial T'/\partial z$ spectrum by dividing the frequency by W and multiplying the spectrum by W. We detected a patch as a segment of $\partial T'/\partial z$ when the 1-30 Hz band-passed variances calculated at 1-s intervals exceeded five times the noise level for the same frequency band. A model noise spectrum derived from quiet portions of the temperature gradient record is removed from the wavenumber spectrum computed over the length of the segment (at least 3m). We obtain χ by fitting the Batchelor's form to the resolved wavenumber band corresponding to

1-30 Hz, of the spectrum using the measured ε for the patch. Using the background temperature gradient derived from the precision temperature profile, this yields an estimate for Cox number and K_T.

Overturns

In a stratified flow the largest scale associated with overturning eddies is the Ozmidov scale, $L_O = (\varepsilon/N^3)^{1/2}$ [*Ozmidov*, 1965]. Local instabilities in the water column can be detected, in practice, using Thorpe scale analysis [*Thorpe*, 1977]. In this process, the profile of density is reordered to a sorted, statically stable profile. The r.m.s. of displacements required for this reordering within an overturn is called the Thorpe scale (L_T): *Dillon* [1982] showed that $L_O=0.8L_T$, thus allowing ε to be inferred from L_T (section 5.1). We detected density overturns using 10-cm averaged σ_θ profiles evaluated from the precision sensors of the microstructure profiler, with a noise threshold set to 0.002 kg m^{-3} determined after run-length tests of *Galbraith and Kelley* [1996]. An additional water-mass test [*Galbraith and Kelley*, 1996] excluded artificial overturn signatures resulting from the presence of different water masses and temperature-salinity sensor mismatch.

Double diffusion

Double diffusive convection (DDC) driven by the difference in molecular diffusivities for heat and salt [*Turner*, 1973] can induce significant vertical fluxes. A prerequisite for DDC is that both temperature and salinity either increase or decrease with depth and is expected for positive values of the density ratio, $R_\rho = (\beta\ \partial S/\partial z)/\ (\alpha\ \partial T/\partial z)$, with $0< R_\rho < 1$ favourable for salt fingering and $R_\rho>1$ for diffusive layering. Here α is the thermal expansion coefficient and β is the haline contraction coefficient. Equivalently, diffusive layering is expected for -90° < Tu < -45° where Turner angle is Tu=arctan[(1 + R_ρ)/(1 - R_ρ)]. The predominant stratification in the Barents Sea with cold and less-saline water overlying warm and salty water is susceptible to diffusive layering.

We identify diffusive layers from temperature profiles recorded by the fast response thermistor, averaged over 10 samples (i.e. ~ 26 Hz), using a histogram approach *[Padman and Dillon, 1988]*. Heat fluxes resulting from the diffusive layers were calculated from

$$F_H = 0.0032\rho_0 c_p \alpha^{-1} \cdot \exp\left[4.8R_\rho^{-0.72}\right] \cdot (gk_T^2 \nu^{-1})^{1/3} \cdot (\alpha \Delta T)^{4/3} \qquad (1)$$

[*Kelley*, 1990], where ρ_0 is the mean density, c_p is the specific heat, g is the gravitational acceleration, k_T is the molecular diffusivity of heat, ν is the viscosity, and ΔT is the temperature difference between adjacent layers. The variability of R_ρ and ΔT across individual steps in a staircase can significantly affect the mean flux relative to that calculated from bulk density ratio and mean ΔT [*Padman and Dillon,* 1987]. In evaluating Eq. (1) we used ΔT for each step and calculated R_ρ using temperature and salinity contrasts between adjacent layers and local α and β.

4 Observations

4.1 Environmental forcing and ice conditions

Ice conditions

Ice concentration maps covering the study site at the beginning of each cruise are shown in Figure 2. Satellite-derived (AMSR-E) sea ice concentration data on 6.25 km grid are used [*Kaleschke et al.*, 2001]. According to the visual observations, the ice cover was between

40-90 % at the drift stations (Table 1), and varied by up to 20 % within the station time depending on wind and currents. Stations were occupied within ~10 nautical miles from the ice edge (defined as the transition to very open drift ice, <10 %). In contrast to the spring 2005 when the southern ice edge reached ~76°N, in July 2004, a large area of open water followed the northern continental shelf slope, and most of the central Barents Sea was ice free (Figure 2).

Tides

Tidal current speed derived from AOTIM (section 3.2) using the four main constituents M_2, S_2, K_1, and O_1 is shown for periods covering each drift station in Figure 3. Predictions are obtained for the mean location of each station during the drift. Tidal currents were very weak at stations VII and XIV, located at the shelf break north of Spitsbergen. Three of the stations occupied in 2004 were during transition from neap to spring tide (Figure 3a). The station depths were shallower for the later of these stations, leading to a large increase in tidal currents despite their geographical proximity. Stations XVI, XVII and XVIII, surveyed in 2005, were in an area with more modest tidal currents and narrower spring-neap range (Figure 3b).

Wind

Measured wind for each cruise is shown in Figure 3c-d. The lowest wind speeds were observed at X and XIII with mean wind work of ~0.5 W m^{-2} (Table 2). All the other stations had considerable energy input from winds, with the largest values found at XIV, XVI and XVIII. At the latter two, microstructure sampling had to be interrupted due to the strong winds.

4.2 Hydrography and currents

In the following, we cluster stations according to their geographical locations and corresponding dominant water masses and large scale current features: the Northern shelf break stations (VII and XIV), the Interior stations (X, XI, XIII), and the Southern MIZ stations (XVI, XVII and XVIII). The corresponding CTD profiles (Figure 4), T-S diagrams (Figure 5), layer and M_2-phase averaged currents (Figure 6) and current profiles along the principal axis ensemble-averaged during flood and ebb (Figure 7) are presented. Station mean properties are given in Table 2.

Northern shelf break stations: VII, XIV

In this area the mean ice and surface water drift is southwest towards the Fram Strait. A layer of Surface Melt Water (SMW) overlies the seasonal pycnocline, atop ArW. The permanent pycnocline separates this from AW, which flows eastwards along the shelf break, following the topography.

Station VII, located north of the steepest part of the shelf slope had a <10 m deep surface mixed layer consisting of near-freezing melt water (Figure 4a). A pronounced halocline reached down to 30 m and temperature remained near freezing to ~50 m, where a transitional zone from ArW to AW started. Both temperature and salinity increased down to ~100 m and remained quasi-uniform with depth. At the shelf slope north of Spitsbergen, station XIV started at the ~2000 m isobath and gradually drifted shelfwards to the 1200 m isobath. D_{mixed} and D_{pyc} were deeper at this station, and temperature remained >-1°C at all depths. Lateral interleaving was observed at depths > 80 m where AW was dominant (Figure 4b). Here, local instabilities, associated with large co-varying fluctuations in temperature and salinity reaching 1°C and 0.2 psu over O(1m), were seen. Although similar in vertical structure, XIV was warmer, more saline and denser than VII in the upper 100 m (Figure 5a).

Surface currents of 20-35 cm s^{-1} at VII, directed south-eastwards (Figure 6a), were mainly wind forced. This station was located north of the core of the AW inflow. The south-south-east net current (time averaged over two M_2 cycles) below the pycnocline was only weakly influenced by tides. At XIV, surface currents towards south-west were clearly wind driven (Figure 6b) while below the pycnocline a large net current to the north-east, with tidal modulations, was observed (Figure 7b).

Interior stations: X, XI, XIII

Located in the northern part of the Barents Sea proper, the interior stations are characterized by Arctic type water (ArW and SMW) through most of the water column, and modified and diluted AW near the bottom in deeper trenches. The general ice and surface drift pattern is to the south-west. Mean pathways of the deeper water are largely unknown.

Of the Interior stations X and XI were relatively deep (300 and 200 m respectively) and were characterized by low-salinity melt water with T > 0 °C (Figure 4c-d) atop a sharp pycnocline extending to 25-30 m with water near freezing before a gradual transition to warmer and more saline water towards the bottom. At the shallower (100 m) station XIII, temperature was uniform with depth, around -0.7 °C, and stratification was controlled by salinity. The main pycnocline was confined to the upper ~40 m, followed by weaker stratification (Figure 4e). The horizontal line in T-S space at this station (Figure 5a) indicates continuous vertical heat exchange. The absence of a vertical temperature gradient suggests that in addition to solar heating, heat was advected in near the bottom. At nearby XI the water at depths > 75 m was warmer than at corresponding depths at XIII, indicating a possible heat source. At X lateral interleaving was seen, particularly between 10-30 m and 50-100 m. As the main characteristics of X and XI are similar, only XI is shown in Figure 5a. Below the temperature minimum at ~50 m the T-S trace follows a mixing line with the AW found north of the shelf break.

Stations X and XI were similar in surface and deep current pattern (Figure 6, Figure 7), however, strong wind at XI (Figure 3) led to strong NNE surface current and enhanced average shear at depths <30 m, corresponding with the base of the pycnocline. At station X, AOTIM-derived tidal phase was comparable to that of the depth-mean ADCP current. The discrepancy in the magnitude of velocity until doy = 209.5 (Figure 8a), i.e., the NE bias in ADCP-derived currents, is caused by a residual current, as seen in the drift path in Figure 8b, likely forced by southerly wind of ~5 m/s during ~24 h preceding the drift. Increasing wind stress by the end of the drift was accompanied by larger current velocities and more intense surface layer shear. An estimate of the relative contribution of dominant semi-diurnal band tides to forcing and variability of currents at each station is made by comparing the semi-diurnal band inferred from AOTIM and depth-averaged ADCP currents. At the latitudes of the survey, the period of inertial oscillations is only ~15 min shorter than the 12.42 h period of the dominant M_2 tide [*Pease et al.*, 1995]. The two can therefore not be separated with confidence through harmonic analysis of the ADCP time series. Assuming that AOTIM results obtained for each station are representative for the tides in the area, we compare the dominant semi-diurnal tides (M_2+S_2) to depth-averaged ADCP current band-passed over a one-hour window centered between the S_2 and M_2 periods, thus covering both the semi-diurnal and the inertial periods. The variance explained by the tides in the semi-diurnal band is summarized in Table 2. At station X, this crude comparison attributes 46% of the variability to tidal currents. When comparing depth-averaged currents to results from a depth-integrated model, in addition to the uncertainty associated with AOTIM results, some uncertainty arises from using ADCP currents covering a fraction of the water column: Near the critical latitude where M_2 period equals the inertial period, the vertical distribution of the current is highly non-uniform [*Nøst*, 1994] and the unresolved fraction of the water column can contribute significantly to the depth average.

During the shallow drift at XIII, bottom depth spanned 50 - 150 m over the complex topography near Kvitøya. Net wind-driven transport was negligible (Figure 6e), and the drift path (not shown) was almost a pure ellipse returning to the same position after one near-inertial (~M_2) cycle. The current reached 50 cm s^{-1} in the upper 50 m, which induced large drag and bottom-enhanced shear above the sea floor at shallows. Current direction rotated CCW with depth part of the time, suggesting upward energy propagation [*Leaman and Sanford*, 1975].

Southern MIZ stations: XVI, XVII, XVIII

The southern part of the Barents Sea is dominated by AW. Here the incoming AW crosses the Polar Front and subducts beneath ice and Arctic type water flowing southwest.

At the ice-free water reference station south of the Polar Front, XVIII, water at all depths was of Atlantic origin (Figure 4h). At the beginning of the station time there was a small density gradient near the surface. The passage of a storm (Figure 3b) mixed down the warmer surface water and homogenized the upper water column. Net depth-averaged current was weak at this station (Figure 6h, Figure 7h).

In the northern part of Hopen Deep, at XVI, below a shallow mixed layer and a main pycnocline extending down to >50 m, the water column was rather homogeneous with AW influence (T>1 °C, S>34.9) (Figure 4f). At the beginning, strong wind from East led to a significant net westerly drift. The principal axis of the depth-averaged current is along 40° true and the mean current profile during floods is negative along this axis, i.e. towards the south-west (Figure 7f). The net current below the pycnocline, however, is to the south-south-east (Figure 6e).

Farther east, at XVII, a deep surface mixed layer was dominated by ArW (Figure 4g), but higher temperature and salinity towards the bottom indicate some intrusion of and mixing with modified AW. Salinity-compensated temperature fluctuations were associated with this horizontal interleaving. Surface currents were shifted westward by wind forcing during the first ~15 h. The net current (i.e., 2 M_2 cycles averaged out) below the pycnocline was small (Figure 6g), comparable to that of the Interior stations. This is consistent with the average current profiles approximately mirroring each other during flood and ebb (Figure 7g).

Although station XVI was not on the direct path from XVIII to XVII, the TS-plot in Figure 5b illustrates the changes that the AW undergoes as it flows north-east in the Barents Sea. At ice-free XVIII, heat exchange with the atmosphere is the only significant modification, as inferred from the vertical line in T-S space. At XVI a less saline and cooler upper layer is seen due to interaction with ice. At the eastern station, XVII, a greater part of the water column had low temperature but the intermediate part of the water column overlaps that of XVI in T-S space. Hydrography at depth > 100 m is similar to the characteristics of modified AW outflow to the Kara Sea (Barents Sea Branch Water, BSBW, $T<0$, $34.7<S<34.9$, as defined by *Schauer et al.* [2002a]). Note that all three stations have nearly identical density at 200 m depth. The enhanced near-bottom salinities at both XVI and XVII indicate advection of brine-enriched water from nearby banks [*Midttun*, 1985].

The surface waters of both XVI and XVII fall within the definition of Cold Halocline Water (CHW) as defined by *Steele et al.* [1995]. *Rudels et al.* [2004] distinguish between the CHW formed near the northern shelf break and that formed near the Polar Front in the central Barents Sea, with the latter being more saline. This difference is seen between the T-S plots in Figure 5a-b. Being closer to the shelf slope when the two branches meet at the St. Anna Trough, the Barents Sea CHW eventually contributes to the lower part of the Arctic Ocean halocline particularly in the Makarov and Canada basins, whereas the WSC branch mainly forms the halocline of the Nansen and Amundsen basins. Contributions to intermediate Arctic Ocean waters from the two AW branches have similar geographical distribution.

4.3 Diapycnal mixing

The dynamics of the upper mixing layer for the 2005 survey is described in *Fer and Sundfjord* [2006]. In contrast to a profile in open water, the mean ε profile under ice was elevated from levels predicted by constant-stress wall scaling within 2.5 times the ice-keel-depth. At the base of the mixing layer below ice, they reported vertical eddy diffusivities of $1\text{-}10\times10^{-4}$ m^2 s^{-1}, with corresponding heat fluxes of 10-20 W m^{-2}.

Here, we focus on mixing within and below the pycnocline. Station-mean dissipation and diffusivity profiles from the upper 60 m (section 3.5), are shown in Figure 9. For each station, average values of ε within ($D_{mixed} < z < D_{pyc}$) and below the pycnocline ($D_{pyc} < z < D_{pyc}+30$) are tabulated in Table 2. The salient features can be described as follows. At all stations but X (below 15 m), ε-profiles were above the noise level of the instrument (Figure 9). Typical K_ρ profiles show large diffusivity, > 10^{-4} m^2 s^{-1}, throughout the water column and exceeding 10^{-3} m^2 s^{-1} for highly turbulent portions. In the upper 15 m at X, where ε is above the noise level, K_ρ is of the order 10^{-5} m^2 s^{-1}, comparable to the open-ocean thermocline levels. This low level of turbulent activity is due to weak wind forcing and ocean current, and strong stratification particularly at the diluted surface layer (Figure 4c). Overall, eddy diffusivities within the pycnocline were greater than below it at all stations, except at stations X and XIII where the wind forcing was negligible. For stronger wind and tidal forcing, dissipation was ~5 fold enhanced in the pycnocline (XIV and XVI).
At XI, where wind forcing was also strong, the surface mixed layer was shallow and a large portion of the wind energy dissipation likely penetrated to the pycnocline yielding average dissipation of 10^{-6} W kg^{-1} within the pycnocline. The largest dissipation within the

pycnocline was observed at the shallow XIII ($\varepsilon = 1.7\times10^{-6}$ W kg^{-1}), influenced by strong tidal currents.

5 Results and discussion

5.1 Overturns

Density overturns in each microstructure profile were identified (section 3.5), applying thresholds for noise and T-S correlations to ensure that the identified overturns were not spurious. On average, more than two overturns were detected per profile at all stations except XVIII.

In the following we evaluate the $L_O \propto L_T$ relationship, i.e. the length scales associated with the largest scale of turbulent eddies in a stratified flow and density overturns. The background buoyancy frequency, N, was calculated using the density gradient from the slope of linear fit of Thorpe-sorted σ_θ against depth within 1-m above and below each overturn. Of the 375 identified overturns with density fluctuations significantly greater than the set noise threshold, 259 satisfied the conditions of the water-mass test and that N was greater than twice its error estimate. Finally 191 overturns had accompanying ε measurement. We also evaluated the density ratio, R_ρ, for each patch, again using vertical gradients derived from linear fits, to delineate diffusive layering favourable overturns. As no significant difference was found between patches with background $R_\rho<0$ or $R_\rho>1$, all 191 overturns were evaluated (Figure 10) to obtain $L_O=(0.7\pm1.1)L_T^{(1.1\pm0.1)}$, where the uncertainties are the standard errors. Stations with higher mean dissipation (XI, XIII) gave somewhat higher estimates for Thorpe scales compared with the less energetic stations. The exponent on L_T is not significantly different than unity, and we obtain a maximum-likelihood estimate from a log-normal distribution of the ratio $r=L_O/L_T$ of 0.9 with 95 % confidence limits [0.8 1.0]. The estimate of r in this work is comparable to previously reported estimates of r = 0.8 (±0.4) in the seasonal oceanic thermocline [*Dillon*, 1982]; r = 0.66 (±0.27) [*Crawford*, 1986] in the permanent oceanic thermocline; r = 0.95 (±0.6) [*Ferron et al.*, 1998] in the Romanche Fracture zone for $\theta< 2°C$; and r = 0.7-1.1 from overflow of a high-latitude sill-fjord [*Fer*, 2006]. We suggest that dissipation in the MIZ of the Barents Sea can be estimated from CTD data with sufficient resolution as $\varepsilon = (rL_T)^2N^3$, using r = 0.9.

5.2 Diffusivity for heat and dissipation ratio

Eddy diffusivity obtained from the Osborn's model (section 3.5) is often calculated using a dissipation ratio $\Gamma = 0.2$, which gives a theoretical upper limit for K_ρ. The parameter Γ is related to the flux Richardson number, R_f, as $\Gamma = R_f/(1-R_f)$ and $\Gamma = 0.2$ follows from the theoretical critical value of $R_f \sim 0.17$ [*Ellison*, 1957]. R_f is also referred to as mixing efficiency and is defined as the ratio of the rate of potential energy change to the work done for turbulent production. The magnitude of the mixing efficiency is reported to depend on the Richardson number, the processes generating the turbulence (e.g. shear production, DDC, grid generated turbulence) [*Linden*, 1979], and more recently differential diffusion [*Jackson and Rehmann*, 2003]. A discussion with respect to patchy oceanic turbulence is given by *Arneborg* [2002] who recommended $R_f = 0.11$ ($\Gamma = 0.12$), a value supported by microstructure measurements [*St Laurent and Schmitt*, 1999]. When dissipation rate of temperature variance, χ, and of TKE, ε, are available through microstructure measurements, the dissipation ratio is typically estimated from $\Gamma \equiv \chi N^2/(2\langle \partial T/\partial z\rangle^2 \varepsilon)$, which is only valid if $K_T = K_\rho$ and conditions for validity of both Osborn-Cox and Osborn models are satisfied [see *Ruddick et al.*, 1997]. The values compiled by *Ruddick et al.* [1997] range from $0 < R_f < 0.26$.

Using Reynolds analogy, when the flow is highly turbulent and when temperature and salinity contribute equally to the stratification, K_ρ is approximately equal to the diffusivities for heat, K_T, or for salt. When the stratification is weak or in the presence of double diffusion Osborn's model can give erroneous results. Recent laboratory results [*Barry et al.*, 2001, BIWI hereafter] and direct numerical simulations [*Shih et al.*, 2005, SKIF hereafter] showed that, for $\varepsilon/\nu N^2 < 1000$, Osborn's model overestimated the measurements with a factor of 2 and for larger $\varepsilon/\nu N^2$ the discrepancy was systematically larger exceeding one order of magnitude for $\varepsilon/\nu N^2 \sim 10^4$. The non-dimensional parameter $\varepsilon/\nu N^2$ is in the form of a Reynolds number and is often referred to as buoyancy Reynolds number or turbulent activity index. BIWI proposed $K_\rho = 17\nu^{2/3} k_T^{1/3} (\varepsilon/\nu N^2)^{1/3}$ for $\varepsilon/\nu N^2 > 800$ (the constant and the threshold is different than those reported in BIWI due to a factor 2.8 error in dissipation measurements [*Jackson and Rehmann*, 2003]). Using a wider range of $\varepsilon/\nu N^2$ SKIF proposed $K_\rho = 2\nu(\varepsilon/\nu N^2)^{1/2}$ for $\varepsilon/\nu N^2 > 100$. Note the scaling with different powers of the buoyancy Reynolds number for the different models. In the following we present independent estimates for diffusivity for heat derived from temperature microstructure, compare to diffusivity of mass inferred from Osborn's model, BIWI and SKIF and estimate the dissipation ratio for the survey area.

We obtained K_T using the Osborn-Cox model (section 3.5) for segments of enhanced temperature gradient variance. Of the 567 detected segments (patches), 407 satisfied the conditions 1) background stratification and temperature gradients are greater than twice the error estimate 2) there are accompanying ε measurements 3) temperature-gradient spectrum acceptably conforms to the Batchelor's form in the resolved wavenumber range and 4) patch is located below the mixed layer. The latter condition is imposed to exclude the effects of significant stabilizing buoyancy flux observed in the mixed layer in response to melting of the ice [*Fer and Sundfjord*, 2006] when the assumptions behind the Osborn-Cox model will not hold. An example of two of the patches, detected at XIV, is given in Figure 11. Each patch is susceptible to diffusive layering with $R_\rho>1$ but the one at about 130 m has Ri ~ 5 and less microstructure shear variance, whereas that at ~30 m has Ri~2.2 with ε five fold larger. The shear spectra from both probes and both patches agree with the Nasmyth's universal form. The dT′/dz spectra are visually consistent with the best-fit Batchelor forms in the resolved wavenumber range, derived using the reliably measured ε. The second patch is just above the AW core and the enhanced temperature microstructure is related to the mixing of heat from AW towards upper layers.

The variation of K_T with the buoyancy Reynolds number is shown in Figure 12 together with expected relations for the Osborn (for K_ρ), SKIF and BIWI models. Values of K_T are comparable to K_ρ estimates using Γ=0.2 (typical value), Γ=0.12 (used in this study) and Γ=0.33 (survey mean value derived using the observations discussed below). There is a robust increase with increasing $\varepsilon/\nu N^2$, consistent with the slope expected from the Osborn model over the observed range of $\varepsilon/\nu N^2$. No significant regime shift is seen around $\varepsilon/\nu N^2 \sim 800$ (BIWI) or ~ 100 (SKIF). Although there is large scatter and measurement uncertainty, $K_T \cong K_\rho \propto \varepsilon/N^2$ scaling describes the observations reasonably well whereas BIWI and SKIF models significantly underestimate K_T for $\varepsilon/\nu N^2 > 1000$. A recent study measured vertical eddy diffusivity directly in an estuary [*Etemad-Shahidi and Imberger*, 2005] and compared with indirect methods of Osborn, Osborn-Cox and BIWI. They reported that best estimates were obtained from Osborn-Cox model whereas BIWI model over-estimated the measurements by a factor of 10, different from our results.

The dissipation ratio $\Gamma \equiv \chi N^2/(2\langle\partial T/\partial z\rangle^2\varepsilon)$ derived from the patches (407 data points in total) cover a range of 0.014 – 9.3 and is log-normally distributed between $\Gamma = 0.01$-1 falling on a straight line in normal probability plot of $\log_{10}(\Gamma)$ (Figure 13a). The probability distribution is calculated from the histogram of $\log_{10}(\Gamma)$ and the distribution in the range $0.01 < \Gamma < 1$ (filled bullets in Figure 13b) is fitted to the lognormal probability density function using a non-linear least squares fit. The mean value of Γ expected from a lognormal distribution is 0.33. This is larger than values reported for typical oceanic conditions, however, it is comparable to the upper range of values compiled in Table 2 of *Ruddick et al.* [1997] ($R_f = 0.25$ yields $\Gamma = 0.33$). The majority of the patches have bulk R_ρ values favourable for double diffusion: 102 patches with $R_\rho < 0$ (diffusively stable) and 305 with $R_\rho > 0$. Regressing $x = \varepsilon/N^2$ against $y = \chi/(2\langle\partial T/\partial z\rangle^2)$ on log-log space we obtain a relation of the form $y = ax^b$. The exponent b is not significantly different than unity for both diffusively stable and unstable conditions (Figure 14), hence the best-fit value of coefficient a is equivalent to the diffusivity ratio equal to 0.2 for the stable cases, but increases to 0.7 for $R_\rho > 0$. The difference is significant at 95% confidence.

Heat flux, $F_H = \rho C_P K_T dT/dz$, where c_p is the specific heat and dT/dz is the background temperature gradient, is calculated for the detected patches and is presented for two representative stations (X and XVII) in Figure 15. Enhanced positive heat fluxes are correlated with Turner angle, $Tu <-50$, susceptible for diffusive layering. Temperature anomalies from the average temperature on the station-mean isopycnal are in excess of ±0.8°C at both stations. Patches of warm intrusions are observed along isopycnals, compensated by salinity.

5.3 Double diffusion

The water column in the MIZ of the Barents Sea was observed to be favorable for double diffusion typically in the upper parts of warm intrusions and below the seasonal pycnocline in the transition zone to AW (see e.g. Turner angle < -45 in Figure 15a and c). At stations where DDC is not dominated by turbulent mixing, step structures indicating diffusive layers were seen (at X, XVII and to some extent at XIV and XVI). Using the method described in section 3.5 we have identified individual steps and calculated resulting heat fluxes based on local density ratio and temperature difference across the steps.

The largest number of diffusive layers was found at Interior station X (see sample profiles in Figure 16), where 19 of 39 profiles contained one or more depth segments with steps fulfilling the criteria for layer height, temperature difference across the step, and that $R_\rho>1$. Diffusive layers with mean thickness of ~0.7 m and mean temperature difference of 0.14°C were found at 40-75 m, between the region of uniformly low temperatures and the transitional layer to AW. The resulting heat fluxes ranged from 0.3 to 33 W m^{-2} (mean 6.3 W m^{-2}).

At the eastern station XVII steps were found at depths >60 m in 15 of the 32 profiles. The layers were typically twice as thick of those at X but with slightly smaller temperature increments. Mean diffusive heat flux was 10.7 W m^{-2}, with maximum values ~50 W m^{-2}.

At stations XIV (northern Shelf Break) and XVI (just north of the Polar Front) fewer diffusive layers were detected, in 7 (of 21) and 3 (of 13) profiles respectively. Their characteristics were similar, with mean heights of ~1.0 m and temperature steps of 0.10°C, all found in the upper part of the AW layers, typically around 60 m depth. Mean heat fluxes were around 3 W m^{-2} and maximum values were in excess of 10 W m^{-2}. These DDC staircases appeared to be of more transient nature than those observed at X and XVII, where the same structure could be detected in several consecutive profiles.

Local diffusive heat fluxes are of comparable magnitude to heat flux calculations from available patches based on the Osborn-Cox model (section 5.2) at stations X and XVII. At X, mean heat flux in active patches was ~15 W m^{-2}, 2.5 times greater than the mean flux through the observed DDC steps. At XVII, mean F_H at depths where DDC was seen to occur (> 60 m) was ~50 W m^{-2}; five times the mean DDC fluxes. Bearing in mind that the overall mean heat fluxes are not resolved and are biased large through averaging over patches of enhanced temperature gradient variance, our data show that in comparison with turbulent heat fluxes, DDC can be important for vertical heat fluxes in areas with moderate or low mechanical stirring and favourable hydrographic conditions. To our knowledge, double-diffusive mixing associated with horizontal intrusions has not previously been reported for the Barents Sea proper, but this process is believed to be dominant for vertical heat fluxes in the quieter parts of the interior Arctic Ocean [e.g. *Padman and Dillon*, 1989; *Carmack et al.*, 1997; *Rudels et al.*, 1999] and in the permanent pycnocline at the slope of the western Weddell Sea [*Robertson et al.*, 1995]. At the deep shelf slope north of Svalbard *Perkin and Lewis* [1984] report heat fluxes of up to O(10) W m^{-2} associated with double diffusion, typically for depth >140 m over bottom depths of 1000-2000 m (see e.g. their station 215, at nearly the same location as our XIV). Their data suggest that more efficient and persistent double-diffusive fluxes can be expected at greater depths than sampled by our profiles.

5.4 Response to forcing

Wind, tides and net currents

In this section we investigate relationships between the observed dissipation within and below the pycnocline, and forcing mechanisms induced by wind and oceanic currents. Using the stations occupied in 2005 *Fer and Sundfjord* [2006] show that the dissipation in the surface mixed layer is significantly correlated with wind stress and that the depth of mixing and the entrainment into the mixed layer scale with under-ice friction velocity, which in turn depends on the wind speed. Since wind energy and associated current shear can protrude beyond the mixed layer it may also be possible to diagnose dissipation of TKE within the pycnocline as a function of wind energy. Significant correlation between depth-integrated dissipation within the pycnocline and the wind speed is found at stations with considerable wind forcing ($E_{10} > 2$ W m^{-2}, i.e. all stations except X and XIII). The relationship is strongest when scaled with the thickness and depth of the pycnocline, implying that a shallow pycnocline is more influenced by the wind. If we assume that the fraction of E_{10} available for mixing decreases linearly with depth from its surface value to zero at the base of the pycnocline, a scaling of the form $\varepsilon_I \propto E_{10} \frac{D_{pyc} - D_{mixed}}{D_{pyc}}$ explains 62 % of the variability when dissipation values varied by a factor 10 and wind work by a factor 3. Here $\varepsilon_I = \int_{D_{mixed}}^{D_{pyc}} \rho\varepsilon(z)dz$ is the dissipation integrated between the base of the mixed layer and the base of the pycnocline.

In the pycnocline, not only the wind-driven shear but also the tides and other currents will contribute to the generation of turbulence. Assuming that a fraction of the total kinetic energy, KE, measured by the ship-ADCP is available for turbulent dissipation in the pycnocline, we seek a correlation between KE per unit mass ($=\frac{1}{2}V^2$, V is current velocity from ADCP) and dissipation within the pycnocline. When scaled by N to account for the varying stratification and to be consistent with units, the relation $\varepsilon \propto \frac{1}{2}V^2N$ represents the variability of the observed mean dissipation with a correlation coefficient $r=0.69$. This is also the case below the pycnocline ($D_{pyc} < z < D_{pyc} + 30$) with $r = 0.85$ derived over all stations.

In the above analysis, parameters derived from station means are used in order to average over several near-inertial or M_2 periods. Therefore the degrees-of-freedom is low due to scarce data points. Correlations, however, are similar when individual sets are used. We avoid proposing specific models for the above relationships, but note that parameters derived from wind measurements and shipborne ADCP provide for crude estimates of the levels of dissipation within and below the pycnocline, complementary to the mixed layer response shown in *Fer and Sundfjord* [2006].

The contribution from tidal currents to mixing can not be confidently assessed through harmonic analysis of short time series of 1-2 days. The comparison of near-inertial (periods covering f, M_2, S_2) band-passed depth-averaged ADCP current and AOTIM semi-diurnal tides (M_2+S_2) (see section 4.2) indicate that tides dominate the variability at stations XI, XVI and XVII (Table 2). At XIII the drift traversed highly variable topography (from 50 to >100 m depth) and was of short duration (~20 hrs). Comparison with AOTIM predictions could therefore not be made with confidence. The absence of significant wind forcing, the nearly elliptical drift pattern, and nearly depth-independent currents indicate that the contribution from tides at XIII are likely large.

Mixing induced by internal waves

One of the mechanisms dissipating turbulent energy is breaking of internal waves. In a deep ocean away from boundaries the amount of turbulent mixing due to internal waves can be estimated using the Garrett-Munk internal wave model spectrum [*Garrett and Munk*, 1975], assuming that the energy is transferred from the frequency and length scales where internal waves are generated to the scales where they break and dissipate. A commonly used model that incorporates easily observable O(10-m) shear and stratification is proposed by *Gregg* [1989]:

$$\varepsilon_{G89} = 7\times10^{-10}\left\langle N^2/N_0^2\right\rangle\left\langle Sh^4/Sh_{GM}^4\right\rangle \qquad (2)$$

where N is the observed buoyancy frequency, $N_0 = 5.24\times10^{-3}\ s^{-1}$ ($\equiv$ 3 cycles per hour) is the canonical deep ocean stratification, Sh^4 is observed squared-shear variance and Sh^4_{GM} is the squared-shear variance of the Garrett-Munk model. The above model, based on modifications on the analytic model by *Henyey et al.* [1986], is a simplified version, referenced to 30° latitude and neglects latitudal dependence. At high latitudes the effect of latitude can be important and we therefore apply the more general, so-called Gregg-Henyey model [*Gregg*, 1989] :

$$\varepsilon_{GH} = 1.7\times10^{-6}\, f\, \cosh^{-1}(N_0/f)\left\langle N^2/N_0^2\right\rangle\left\langle Sh^4/Sh^4_{GM}\right\rangle \tag{3}$$

where f is the local Coriolis parameter.

MacKinnon and Gregg [2003a] proposed an alternative dissipation scaling for shallow shelf application based on low-passed fine scale shear:

$$\varepsilon_{MG} = \varepsilon_0 (N/N_0)(Sh/Sh_0) \tag{4}$$

Here, ε_0 is a constant typically chosen to match the survey average, Sh is shear and Sh_0 is reference shear level (MacKinnon and Gregg applied $Sh_0 = N_0$, for simplicity). This scaling assumes that the low-mode “background” shear is decoupled from higher-mode waves.

Because the water column is stratified below D_{mixed} (the mixed bottom boundary layer is not resolved), internal waves can be supported and we apply the above models, accordingly, below the mixed layer from the first depth at which 16-m shear is available. We used 16-m finite differenced shear calculated from ADCP data, and applied a correction factor of 2.26 and 2.61, from 4-m and 8-m bin sizes, respectively, for attenuation of the shear variance spectrum due to ADCP bin size and finite difference interval length

[*Gregg and Sanford*, 1988; *Wijesekera et al.*, 1993]. The ratio of the observed dissipation to that inferred from the models (Eq. 3-4) are given in Table 3, together with the stratification and shear variance with respect to the GM levels. $\mathrm{Sh}^2_{\mathrm{GM}}$ is approximated from Eq. A11 of *Gregg and Kunze* [1991] for a cutoff vertical wavenumber corresponding to 16 m. In evaluating $\varepsilon_{\mathrm{MG}}$, we use $\varepsilon_0 = 4.5\times10^{-8}$ W kg^{-1}, the maximum likelihood estimate of all dissipation measurements below D_{mixed}. The open-ocean internal wave models do not reproduce the observations satisfactorily. The profiles of the ratio of observed to inferred dissipation are presented for $\varepsilon_{\mathrm{GH}}$ and $\varepsilon_{\mathrm{MG}}$ in Figure 17a, together with the distribution in $N^2 - \mathrm{Sh}^2$ space Figure 17b-d), following *MacKinnon and Gregg* [2003a] and *Carter et al.* [2005]. The predictions from the Gregg-Henyey model do not agree with our observations, whereas the pattern (in $N^2 - \mathrm{Sh}^2$ space) resulting from the MacKinnon and Gregg scaling compare reasonably well with the data set. The observed variability of ε is better captured by $\varepsilon \propto N\mathrm{Sh}$ consistent with the $K_\rho \propto N^{-1}$ scaling appropriate for lakes and fjords [*Gargett and Holloway*, 1984; *D'Asaro and Lien*, 2000; *Fer et al.*, 2004; *Fer*, 2006]. A good agreement with the internal wave-wave interaction models and the observations is expected only if the mixing is pre-dominantly due to internal waves, which is not the case in our survey where mean shear is also important. We cannot assess the contribution of internal wave induced mixing relative to that induced by mean shear because the observations are uncorrelated with the Gregg-Henyey model. The fairly good agreement with the MacKinnon and Gregg model, on the other hand, can be fortuitous and not entirely representative of mixing due to wave-wave interaction, because the employed survey mean ε_0 clearly comprises dissipation induced by mean shear as well as other processes.

Internal waves dissipating energy near the pycnocline are mostly generated elsewhere. Inertial waves are typically generated at the surface and have downward energy propagation. Internal waves generated by flow interacting with topography or those reflecting from the bottom will have upward propagating energy. This is manifested in the clockwise (CW) and counter-clockwise (CCW) rotary component vertical wavenumber spectra of shear or velocity, where an excess of CW (in the Northern hemisphere) at low wavenumbers indicates downward propagating near-inertial energy [*Kunze and Sanford*, 1984]. The CW/CCW variance ratios evaluated at the lowest resolved wavenumber of the station averaged velocity spectra are given in Table 3. The ratios suggest that there is upward propagating low-mode internal wave energy at stations XI and XIII near Kvitøya where large tidal flow and enhanced mixing was observed, and to a lesser extent east of the Great Bank, at XVII. The observed levels of mixing can be associated with generation of internal waves over steep topography, comparable to the observations of *Padman and Dillon* [1991] at the deep shelf slope at the northern edge of the Yermak Plateau, north of Spitsbergen. They found highest ε to be correlated with the diurnal tide, interacting with steep topography at the shelf slope and generating internal waves.

6 Implications

6.1 Water mass modification

At station XIV, at the northern shelf break, ε was large within the pycnocline and decayed with depth. Heat fluxes were thus modest in the rather strong mean vertical temperature gradient between the base of the pycnocline and top of the AW (~100 m) (Figure 4b).

Patches of enhanced temperature gradient variance (section 5.2) had mean upward heat flux of ~50 W m^{-2}, with peak values in excess of 200 W m^{-2}. As the WSC continues its flow north-eastwards along the slope, a heat sink is continuously available as more ice and cold surface water is encountered. By losing sufficient heat, the near-surface water at XIV can obtain the same temperature-salinity characteristics as the CHW observed farther north at station VII (Figure 5a), north of the shelf break. Although the modified AW at drift stations XVI and XVII was colder than that at XIV, significant upward heat fluxes were found also in this southern MIZ area. At station XVI, just north of the Polar Front in the central Barents Sea, mean upward fluxes of 16 W m^{-2} were seen in active patches below the pycnocline. Following the Barents Sea branch of AW further en route to the Kara Sea, heat fluxes at XVII larger than +/- 10 W m^{-2} were found at the top/bottom of warm intrusions between 50-150 m, with a net upward heat flux of ~2 W m^{-2}. Due to this heat loss from the modified AW, the near-bottom waters at station XVII can attain the characteristics of BSBW (Figure 5b) without further admixture of high-salinity water.

The relatively deep stations in the Interior MIZ (X and XI) were surveyed in late July 2004, when the surface water was relatively warm (Figure 4d). As a result the cold ArW layer (20-50 m depth) at X received downward heat fluxes of 15 W m^{-2} from above, in addition to upward fluxes of ~20 W m^{-2} from the warm AW below. A similar pattern with pulses of up to one order of magnitude larger fluxes was observed at station XI, where turubulence was more intense. The opposing heat fluxes will warm and homogenize the vertical temperature distribution as the melting season progresses, and the sub-surface water is not likely to attain the characteristics of CHW during summer in this part of the Barents Sea.

6.2 Temporal evolution of stratification

Vigorous mixing implies a downward flux of buoyancy by moving less dense water downwards and heavy water upwards [*Gregg*, 1987]. To maintain stratification, addition of buoyancy in the surface mixed layer by reduction of salinity and/or solar heating is necessary to compensate for this buoyancy loss. During melting of sea ice the buoyancy flux is downwards [*McPhee*, 1990] and might aid in maintaining the stratification against strong mixing. As an illustration, we make sample calculations using observations from station XIII. For $K_\rho \sim O(10^{-3})$ m^2 s^{-1} and a density gradient across the pycnocline of ~0.02 kg m^{-4}, the mass flux through the pycnocline, $K_\rho d\rho/dz = 2\times10^{-5}$ kg m^{-2} s^{-1}, or ~1.7 kg m^{-2} day^{-1}. This must be compensated for by the release of meltwater and/or heating of the surface water. Assuming a pre-melting surface salinity of 34, after a melt period of 30 days the mean rate of density loss from 1.5 m thick ice with salinity of 6 is about 1.2 kg m^{-2} day^{-1}, comparable to the vertical diffusion through the pycnocline. Following the completion of melting, the pycnocline will be eroded unless compensated by density reduction at the surface by thermal expansion of water through solar heating. Assuming a temperature increase of 5 °C (from -1.8 to 3.2 °C) in 30 days for a 10 m thick surface layer, the resulting density reduction rate is 0.1 kg m^{-2} day^{-1}, not enough to maintain a strong post-melt stratification. The turbulence dissipation rate used above is from near spring tide and during part of the lunar cycle the forcing will be weaker. Nevertheless, even a considerably smaller diffusivity will be large enough to erode stratification after all ice has melted, and a new, reduced density gradient must balance vertical fluxes with the buoyancy production. At stations with weaker turbulence, e.g. nearby station X, the vertical mixing will be suppressed by the excess buoyancy produced by melting [see *Fer and Sundfjord*, 2006] and the surface mixed layer will become increasingly diluted and warm as melting and solar heating continues.

6.3 Nutrient fluxes and primary production

After the first seasonal bloom, nutrients in the surface mixed layer are depleted and subsequent primary production in the surface layer of the Barents Sea is often controlled by the vertical flux of nutrients, supplied from below through mixing. Substantial production may also take place within the pycnocline where, after the intense first bloom phase, a chlorophyll *a* maximum is often observed. The position and extent of this maximum within the pycnocline is influenced by the vertical mixing efficiency, as well as other factors, e.g., light penetration depth [*Sakshaug*, 1997; *Reigstad et al.*, 2002; *Sakshaug*, 2004].

Profiles of concentrations of nutrients (nitrate, phosphate and silicate), chlorophyll *a*, and bacterial biomass for the CABANERA drift stations are given in *Sturluson et al.* (Bacterial abundance, biomass and production during spring bloom in the northern Barents Sea, submitted to *Marine Biology Research*, hereafter referred to as *Sturluson et al*., submitted manus.). As an example of how turbulence controls the vertical nutrient flux we contrast two nearby stations with very different turbulence intensities: X and XIII. At station X, using $K_\rho \sim 1.0\times10^{-5}$ m^2 s^{-1} (Table 2) and nitrate concentration gradient between the surface and sub-pycnocline layers of $dC/dz = 10$ mg m^{-4} (approximated from Table 4 and Figure 3 in *Sturluson et al.*, (submitted manus)), the nitrate flux is $K_\rho dC/dz = 1.0\times10^{-4}$ mg nitrate m^{-2}s^{-1}, or ~9 mg nitrate m^{-2} day^{-1}. At station XIII diffusivity at the pycnocline was ~100 times larger. Using the observed, considerably smaller, nitrate gradient of ~2.0 mg m^{-4}, a flux of 150 mg m^{-2} day^{-1}, about 15 times greater than at X, would be expected. The contrast between the two stations in terms of vertical distribution of nutrients and biomass of phytoplankton and bacteria is substantial [*Sturluson et al.* (submitted manus.)]. Nitrate was nearly depleted in the upper ~10 m of both stations. However, while the concentration at X reached 10 μM at 100 m it was only 4 μM at XIII, indicating considerable upward transport here. A small peak in chlorophyll *a* observed in the pycnocline of X was absent at XIII, likely due to rapid vertical mixing. Bacterial production and biomass was found to be 5-10 times greater at XIII and almost evenly distributed throughout the water column, as opposed to being confined mostly to the pycnocline at X.

Similar comparisons for the other stations of the CABANERA surveys also show agreement between the measured profiles of nutrients and primary production/bacterial biomass, and what one would expect from observed vertical mixing and hydrography. The approach used above has previously been shown to give estimates of new production in agreement with values inferred from *in vivo* incubation experiments [*Law et al.*, 2001].

6.4 Implications for carbon uptake

Net sequestration of CO_2 in both inorganic and biological form can take place in the Barents Sea MIZ. According to *Omar et al* [2003], the partial pressure of CO_2 of AW entering the Barents Sea is in equilibrium with the atmosphere. During winter, the solubility of CO_2 in the cold surface layer increases and more CO_2 can be absorbed as the AW transits the Barents Sea. *Kaltin et al.* [2002] found this cooling effect to be more important than the biological uptake from late winter to early summer in the Barents Sea. Our measurements suggest that mixing and heat loss can be large enough to form Cold Halocline Water both around the WSC and along the southern perimeter of the MIZ late in the season (May-July), and such formation is also expected during winter and spring when CO_2 concentrations are potentially highest. Inorganic carbon concentrations for the survey are not available at present. We therefore cannot assess the efficiency of the inorganic pump directly. Nevertheless, we note that the response time for equilibrating a difference in partial pressure of CO_2 between surface water and atmosphere depends on the diffusivity within the upper ocean which is shown to vary significantly with turbulence forcing.

During the productive season, carbon is utilized for primary production and inorganic carbon concentrations in the upper ocean are reduced, accordingly. The under-saturated surface water can thus efficiently absorb CO_2 from the atmosphere, at least until the onset of freezing in early winter. Part of the biologically absorbed carbon is transported from the surface into deeper waters by sinking and diffusion, where it may be buried in the sediments, or remineralized in the sediments or in the water column, potentially increasing the local CO_2 content. As seen at our stations along the AW route towards the Kara Sea, formation of Barents Sea Branch Water, which can later enter the Arctic Ocean below the halocline, can take place also during the productive season. This water mass can thus be enriched in carbon by remineralization of particulate organic carbon sinking from the upper-ocean primary production and is likely to capture and export CO_2 throughout the year, with either the inorganic or biological pump being dominant. Sediment burial within the Barents Sea will depend on distribution and vertical export of primary production, which is linked to the local strength of turbulent mixing.

7 Summary

Measurements of hydrography, currents and turbulence were made in late July 2004 and late May 2005 at drifting ice stations in the MIZ of the Barents Sea, covering a broad range of forcing conditions. The microstructure shear measurements within and below the pycnocline show high, and highly variable, ε values. Turbulent kinetic energy is primarily generated by wind and/or tides at most stations, with the notable exception of station XIV where substantial shear was induced by the surface drift opposing the deeper AW current. At stations with less kinetic energy, double diffusion can give significant heat fluxes when the hydrography is favorable. The diffusive layers detected from high-resolution temperature profiles were O(1m) thick and will not be detectable by conventional CTD surveys. Dissipation ratio, Γ, and mixing efficiency estimates from patches of temperature microstructure where both dissipation of TKE and dissipation of temperature variance were measured are log-normally distributed with a mean value about 50% larger than values typically used for shear measurements. An inspection with respect to R_ρ suggests that for diffusively stable conditions Γ approaches the widely used value of 0.2 and increases threefold for double-diffusion favorable patches. Comparison with turbulent length scales inferred independently from density overturns supports the generally high levels of dissipation. Within the seasonal pycnocline, station-mean ε is $\sim 3\times10^{-8}$ W kg^{-1} in low-energy areas and $>1\times10^{-6}$ W kg^{-1} in areas with strong forcing. Corresponding diffusivity values range from $K_\rho \sim 1\times10^{-5}$ m^2 s^{-1}, comparable to the 'background' diffusivity found in the deeper open ocean pycnocline, to 1-5$\times10^{-3}$ m^2 s^{-1} in energetic areas. Below the pycnocline the dissipation of turbulent kinetic energy is generally smaller (1-30$\times10^{-8}$ W kg^{-1}) and despite the stratification being weaker the resulting diffusivities are lower than within the pycnocline at most stations. Upward propagating energy was inferred over rough topography near Kvitøya. Given the observed bottom-enhanced mixing and strong tidal currents we expect internal tide generation at this site. When tuned with a representative survey mean dissipation, the *MacKinnon and Gregg* [2003a] model reproduced the observed variability of dissipation with depth and in stratification-shear space fairly well. Although utilized to describe the mixing due to internal wave-wave interaction mechanisms, the appropriate scaling of MacKinnon and Gregg can be representative of the observed mixing in the Barents Sea MIZ when tuned with a mean dissipation level representative of all processes at play - which in turn can be adoptable in regional numerical model studies. Future field work with thorough spatial and temporal sampling of both fine structure and microstructure is needed to corroborate our relatively scarce observations and interpretation.

Acknowledgements

We thank Captain Hansen and the crew of R/V Jan Mayen, and cruise leader P. Wassmann for their efforts. We also thank R. Thomson, M. Krassovski and R. Hourston for providing processing routines and documentation for the updated version of the S-M method. Helpful comments and suggestions of two anonymous reviewers are gratefully acknowledged. This work was supported by the Norwegian Research Council project grants 155936/S30, project ‘CABANERA’, and grant 155923/700, ‘ProClim’. This is publication No XXXX of the Bjerknes Centre for Climate Research.

References

Aadlandsvik, B., and H. Loeng (1991), A Study of the Climatic System in the Barents Sea, *Polar Research*, *10* (1), 45-49.

Arneborg, L. (2002), Mixing Efficiencies in Patchy Turbulence, *Journal of Physical Oceanography*, *32* (5), 1496–1506.

Barry, M.E., G.N. Ivey, K.B. Winters, and J. Imberger (2001), Measurements of diapycnal diffusivities in stratifed fluids, *Journal of Fluid Mechanics*, *442*, 267-291.

Carmack, E. (1990), Large scale physical oceanography of polar oceans, in *Polar oceanography, part A: Physical Science*, edited by W.O. Smith, pp. 171-222, Academic Press, New York.

Carmack, E.C., K. Aagaard, J.H. Swift, R.W. MacDonald, F.A. McLaughlin, E.P. Jones, R.G. Perkin, J.N. Smith, K.M. Ellis, and L.R. Killius (1997), Changes in temperature and tracer distributions within the Arctic Ocean: Results from the 1994 Arctic Ocean section, *Deep-Sea Research Part II*, *44* (8), 1487-1502.

Carter, G.S., M.C. Gregg, and R.C. Lien (2005), Internal waves, solitary-like waves, and mixing on the Monterey Bay shelf, *Continental Shelf Research*, *25* (12-13), 1499-1520.

Crawford, G., L. Padman, and M. McPhee (1999), Turbulent Mixing in Barrow Strait, *Continental Shelf Research*, *19*, 205-245.

Crawford, W.R. (1986), A comparison of length scales and decay times of turbulence in stably stratified flows, *Journal of Physical Oceanography*, *16* (11), 1847-1854.

D'Asaro, E.A., and R.C. Lien (2000), The wave-turbulence transition for stratified flow, *Journal of Physical Oceanography*, *30* (7), 1669-1678.

Dillon, T.M. (1982), Vertical Overturns: A Comparison of Thorpe and Ozmidov Length Scales, *Journal of Geophysical Research*, *87* (C12), 9601-9613.

Dillon, T.M., and D.R. Caldwell (1980), The Batchelor spectrum and dissipation in the upper ocean, *Journal of Geophysical Research*, *85* (C4), 1910-1916.

Ellison, T.H. (1957), Turbulent transport of heat and momentum from an infinite rough plane, *Journal of Fluid Mechanics*, *2*, 456-466.

Etemad-Shahidi, A., and J. Imberger (2005), Vertical eddy diffusivity estimations in Swan River Estuary, *Dynamics of Atmospheres and Oceans*, *39* (3-4), 175-187.

Fer, I. (2006), Scaling turbulent dissipation in an Arctic fjord, *Deep-Sea Research - II*, *53* (1-2), 77-95.

Fer, I., R. Skogseth, and P.M. Haugan (2004), Mixing of the Storfjorden overflow (Svalbard Archipelago) inferred from density overturns, *Journal of Geophysical Research-Oceans*, *109* (C1).

Fer, I. and Sundfjord, A., 2006. Observations of upper ocean boundary layer dynamics in the marginal ice zone. *Journal of Geophysical Research-Oceans*, accepted after minor revisions.

Ferron, B., H. Mercier, K. Speer, A.E. Gargett, and K.L. Polzin (1998), Mixing in the Romanche Fracture Zone, *Journal of Physical Oceanography*, *28* (10), 1929–48.

Galbraith, P.E., and D.E. Kelley (1996), Identifying Overturns in CTD Profiles, *Journal of Atmospheric and Oceanic Technology*, *13*, 688-702.

Gargett, A.E., and G. Holloway (1984), Dissipation and diffusion by internal wave breaking, *Journal of Marine Research*, *42*, 15-27.

Garrett, C., and W. Munk (1975), Space-time scales of internal waves: A progress report, *Journal of Geophysical Research*, *80* (3), 291-297.

Gathman, S.G. (1986), Climatology, in *The Nordic seas*, edited by B.G. Hurdle, pp. 1-18, Springer-Verlag, New York.

Gregg, M.C. (1987), Diapycnal Mixing in the Thermocline: A Review, *Journal of Geophysical Research-Oceans*, *92* (C5), 5249-5286.

Gregg, M.C. (1989), Scaling Turbulent Dissipation in the Thermocline, *Journal of Geophysical Research-Oceans*, *94* (C7), 9686-9698.

Gregg, M.C., and E. Kunze (1991), Shear and Strain in Santa Monica Basin, *Journal of Geophysical Research*, *96* (C9), 16709-16719.

Gregg, M.C. and Meagher, T.B., 1980. The dynamic response of glass rod thermistors. *Journal of Geophysical Research*, *85* (C5): 2779-2786.

Gregg, M.C., and T.B. Sanford (1988), The Dependence of Turbulent Dissipation on Stratification in a Diffusively Stable Thermocline, *J. Geophys. Res.*, *93* (C10), 12381-12392.

Guest, P.S., J.W. Glendening, and K.L. Davidson (1995), An observational and numerical study of wind stress variations within marginal ice zones, *Journal of Geophysical Research*, *100* (C6), 10887-10904.

Henyey, F., J. Wright, and S.M. Flatté (1986), Energy and action flow through the internal wave field: An eikonal approach, *Journal of Geophysical Research*, *91* (C7), 8487-8495.

Inall, M.E., T.P. Rippeth, and T.J. Sherwin (2000), Impact of nonlinear waves on the dissipation of internal tidal energy at a shelf break, *Journal of Geophysical Research-Oceans*, *105* (C4), 8687-8705.

Jackson, P.R., and C.R. Rehmann (2003), Laboratory Measurements of Differential Diffusion in a Diffusively Stable, Turbulent Flow, *Journal of Physical Oceanography*, *33* (8), 1592–1603.

Kaleschke, L., C. Lüpkes, T. Vihma, J. Haarpaintner, A. Bochert, J. Hartmann, and G. Heygster (2001), SSM/I Sea Ice Remote Sensing for Mesoscale Ocean-Atmosphere Interaction Analysis, *Canadian Journal of Remote Sensing*, *27* (5), 526-537.

Kaltin, K., L.G. Anderson, K. Olsson, A. Fransson, and M. Chierici (2002), Uptake of atmospheric carbon dioxide in the Barents Sea, *Journal of Marine Systems*, *38* (1-2), 31-45.

Kelley, D.E. (1990), Fluxes Through Diffusive Staircases: A New Formulation, *Journal of Geophysical Research*, *95* (C3), 3365-3371.

Kowalik, Z., and A.Y. Proshutinsky (1994), The Arctic Ocean tides, in *The Polar Oceans and Their Role in Shaping the Global Environment: The Nansen Centennial Volume*, edited by O. Johannessen, R.D. Muench, and J.E. Overland, pp. 137-158, AGU, Washington DC.

Kowalik, Z., and A.Y. Proshutinsky (1995), Topographic enhancement of tidal motion in the western Barents Sea, *Journal of Geophysical Research*, *100* (C2), 2613-2637.

Kunze, E., and T.B. Sanford (1984), Observations of Near-Inertial Waves in a Front, *Journal of Physical Oceanography*, *14* (3), 566-581.

Law, C.S., A.P. Martin, M.I. Liddicoat, A.J. Watson, K.J. Richards, and E.M.S. Woodward (2001), A Lagrangian SF6 tracer study of an anticyclonic eddy in the North Atlantic: patch evolution, vertical mixing and nutrient supply to the mixed layer, *Deep-Sea Research*, *48*, 705-724.

Leaman, K.D., and T.B. Sanford (1975), Vertical Energy Propagation of Inertial Waves: A Vector Spectral Analysis of Velocity Profiles, *J. Geophys. Res.*, *80* (15), 1975-1978.

Linden, P.F. (1979), Mixing in stratified fluids, *Geophys. Astrophys. Fluid Dyn.*, *13*, 3-23.

Loeng, H. (1991), Features of the Physical Oceanographic Conditions of the Barents Sea, *Polar Research*, *10* (1), 5-18.

MacKinnon, J.A., and M.C. Gregg (2003a), Mixing on the Late-Summer New England Shelf - Solibores, Shear and Stratification, *Journal of Physical Oceanography*, *33* (7), 1476-1492.

MacKinnon, J.A., and M.C. Gregg (2003b), Shear and Baroclinic Energy Flux on the Summer New England Shelf, *Journal of Physical Oceanography*, *33* (7), 1462-1475.

McPhee, M. (1990), Small Scale Processes, in *Polar Oceanography, part A: Physical Science*, edited by W.O. Smith, pp. 287-334, Academic Press, New York.

McPhee, M., and T.P. Stanton (1996), Turbulence in the statically unstable oceanic boundary layer under Arctic leads, *Journal of Geophysical Research*, *101* (C3), 6409-6428.

Midttun, L. (1985), Formation of Dense Bottom Water in the Barents Sea, *Deep-Sea Research*, *32* (10), 1233-1241.

Morison, J.H., M. McPhee, and G.A. Maykut (1987), Boundary Layer, Upper Ocean, and Ice Observations in the Greenland Sea Marginal Ice Zone, *Journal of Geophysical Research*, *92* (C7), 6987-7011.

Mosby, H. (1938), Svalbard Waters, *Geofysiske Publikasjoner*, *12* (4), 1-85.

Moum, J.N. (1996), Efficiency of mixing in the main thermocline, *J. Geophys. Res.*, *101* (12), 12,057-12,069.

Moum, J.N., M.C. Gregg, R.C. Lien, and M.E. Carr (1995), Comparison of turbulent kinetic energy dissipation rate estimates from two ocean microstructure profilers, *Journal of Atmospheric and Oceanic Technology*, *12* (2), 346-366.

Moum, J.N., and R.G. Lueck (1985), Causes and implications of noise in oceanic dissipation measurements, *Deep-Sea Research*, *32* (4), 379-390.

Nøst, E. (1994), Calculating tidal current profiles from vertically integrated models near the critical latitude in the Barents Sea, *Journal of Geophysical Research-Oceans*, *99* (C4), 7885-7901.

Oakey, N.S. (1982), Determination of the Rate of Dissipation of Turbulent Energy from Simultaneous Temperature and Velocity Shear Microstructure Measurements, *Journal of Physical Oceanography*, *12* (3), 256-271.

Omar, A., T. Johannessen, K. Kaltin, and A. Olsen (2003), Anthropogenic increase of oceanic pCO2 in the Barents Sea surface water, *J. Geophys. Res.*, *108* (C12), 3388, doi:10.1029/2002JC001628.

Osborn, T.R. (1980), Estimates of the Local Rate of Vertical Diffusion from Dissipation Measurements, *Journal of Physical Oceanography*, *10* (1), 83-89.

Osborn, T.R., and C.S. Cox (1972), Oceanic Fine Structure, *Geophysical Fluid Dynamics*, *3*, 321-345.

Ozmidov, R.V. (1965), On the turbulent exchange in a stably stratified ocean, *Atmospheric and Oceanic Physics*, *8*, 853-860.

Padman, L., and T.M. Dillon (1987), Vertical Heat Fluxes Through the Beaufort Sea Thermohaline Staircase, *Journal of Geophysical Research*, *92* (C10), 10799-10806.

Padman, L., and T.M. Dillon (1988), On the horizontal extent of thermohaline steps in the Canada Basin, *Journal of Physical Oceanography*, *18* (10), 1458-1462.

Padman, L., and T.M. Dillon (1989), Thermal microstructure and internal waves in the Canada Basin diffusive staircase., *Deep-Sea Research*, *36*, 531-542.

Padman, L., and T.M. Dillon (1991), Turbulent Mixing Near the Yermak Plateau During the Coordinated Eastern Arctic Experiment, *Journal of Geophysical Research-Oceans*, *96* (C3), 4769-4782.

Padman, L., and L. Erofeeva (2004), A barotropic inverse tidal model for the Arctic Ocean, *Geophysical Research Letters*, *31* (2), L02303, doi:10.1029/2003GL019003.

Pease, C.H., P. Turet, and R.S. Pritchard (1995), Barents Sea tidal and inertial motions from Argos ice buoys during the Coordinated Eastern Arctic Experiment, *Journal of Geophysical Research*, *100* (C12), 24,705-24,718.

Perkin, R.G., and E.L. Lewis (1984), Mixing in the West Spitsbergen Current, *Journal of Physical Oceanography*, *14* (8), 1315-1325.

Pfirman, S.L., D. Bauch, and T. Gammelsrød (1994), The Northern Barents Sea: Water Mass Distribution and Modification, in *The Polar Oceans and Their Role in Shaping the Global Environment: The Nansen Centennial Volume*, edited by O.M. Johannessen, R.D. Muench, and J.E. Overland, pp. 77-94, AGU, Washington DC.

Prandke, H., and A. Stips (1998), Test measurements with an operational microstructure-turbulence profiler: Detection limit of detection rates, *Aquatic Sciences*, *60*, 191-209.

Rehmann, C.R., and J.R. Koseff (2004), Mean potential energy change in stratified grid turbulence, *Dynamics of Atmospheres and Oceans*, *37* (4), 271–294.

Reigstad, M., P. Wassmann, C. Wexels Riser, S. Øygarden, and F. Rey (2002), Variations in hydrography, nutrients and chlorophyll *a* in the marginal ice-zone and the central Barents Sea, *Journal of Marine Systems*, *38* (1-2), 9-29.

Robertson, R., L. Padman, and M.D. Levine (1995), Fine structure, microstructure, and vertical mixing processes in the upper ocean in the western Weddell Sea, *Journal of Geophysical Research*, *100* (C9), 18,517-18,535.

Ruddick, B.R., D. Walsh, and N.S. Oakey (1997), Variations in Apparent Mixing Efficiency in the North Atlantic Central Water, *Journal of Physical Oceanography*, *27* (12), 2589–2605.

Rudels, B., G. Bjork, R.D. Muench, and U. Schauer (1999), Double-diffusive layering in the Eurasian Basin of the Arctic Ocean, *Journal of Marine Systems*, *21*, 3-27.

Rudels, B., E.P. Jones, U. Schauer, and P. Eriksson (2004), Atlantic sources of the Arctic Ocean surface and halocline waters, *Polar Research*, *23* (2), 181–208.

Sakshaug, E. (1997), Biomass and productivity distributions and their variability in the Barents Sea, *ICES Journal of Marine Science*, *54*, 341-350.

Sakshaug, E. (2004), Primary and Secondary Production in the Arctic Seas, in *The Organic Carbon Cycle in the Arctic Ocean*, edited by R. Stein, and R.W. MacDonald, pp. 57-81, Springer, Berlin-Heidelberg.

Saloranta, T.M., and P.M. Haugan (2001), Interannual variability in the hydrography of Atlantic water northwest of Svalbard, *Journal of Geophysical Research-Oceans*, *106* (C7), 13931-13943.

Schauer, U., H. Loeng, B. Rudels, V.K. Ozhigin, and W. Dieck (2002a), Atlantic Water flow through the Barents and Kara Seas, *Deep-Sea Research I*, *49* (12), 2281-2298.

Schauer, U., B. Rudels, E.P. Jones, L.G. Anderson, R.D. Muench, G. Bjork, J.H. Swift, V. Ivanov, and A.M. Larsson (2002b), Confluence and redistribution of Atlantic Water in the Nansen, Amundsen and Makarov basins, *Ann. Geophysicae*, *20* (2), 257-273.

Shih, L.H., J.R. Koseff, G.N. Ivey, and J.H. Ferziger (2005), Parameterization of turbulent fluxes and scales using homogeneous sheared stably stratified turbulence simulations, *Journal of Fluid Mechanics*, *525*, 193–214.

St Laurent, L.C., and R.W. Schmitt (1999), The Contribution of Salt Fingers to Vertical Mixing in the North Atlantic Tracer Release Experiment, *Journal of Physical Oceanography*, *29* (7), 1404–1424.

Steele, M., J.H. Morison, and T.B. Curtin (1995), Halocline Water Formation in the Barents Sea, *Journal of Geophysical Research-Oceans*, *100* (C1), 881-894.

Thomson, R.E., and I. Fine (2003), Estimating Mixed Layer Depth from Oceanic Profile Data, *Journal of Atmospheric and Oceanic Technology*, *20* (2), 319-329.

Thorpe, S.A. (1977), Turbulence and mixing in a Scottish loch, *Philosophical Transactions of the Royal Society of London Series a-Mathematical Physical and Engineering Sciences*, *286*, 125-181.

Turner, J.S. (1973), *Buoyancy effects in fluids*, 351 pp., Cambridge University Press, New York.

Wijesekera, H.W., T.M. Dillon, and L. Padman (1993), Some Statistical and Dynamical Properties of Turbulence in the Oceanic Pycnocline, *Journal of Geophysical Research-Oceans*, *98* (C12), 22665-22679.

Yamazaki, H., and T. Osborn (1990), Dissipation Estimates for Stratified Turbulence, *Journal of Geophysical Research-Oceans*, *95* (C6), 9739-9744.

Table 1. Survey overview. Latitude, longitude and bottom depth is given for the start of each station. The number of CTD and MSS profiles at each station is given in the last two rows. The number of MSS sets is also indicated in the last row (profiles/sets).

Station	**VII**	**X**	**XI**	**XIII**	**XIV**	**XVI**	**XVII**	**XVIII**
Latitude (N)	82° 24.9	79° 22.7	79° 49.4	79° 56.3	81° 07.6	77° 08.4	77° 25.7	75° 40.5
Longitude (E)	29° 26.2	28° 41.6	29° 43.6	30° 56.6	16° 19.0	29° 56.7	41° 02.8	31° 47.8
Start (doy / year)	204.1/04	206.5/04	210.5/04	212.6/04	139.2/05	144.2/05	147.0/05	149.9/05
Bottom depth (m)	3500	300	200	100	2000	200	220	340
Ice cover (%)	80	40-50	40	30-40	50	80-90	60-70	0
Ice thickness (m)	0.5	1.4	4.0	1.5	1.0	1.0	3.1	-
ADCP duration (h)	22.6	35.5	31.0	20.1	28.2	34.9	37.2	43.2
CTD	4	9	11	5	14	15	14	10
MSS	10/2	39/9	27/6	23/5	21/7	13/5	32/11	15/5

Table 2. Station-mean observations. D_{mixed} is the depth of surface mixed layer, D_{pyc} is the base of the pycnocline, and E_{10} is the wind work at 10 m height. Variance of the observed sub-surface current explained by semi-diurnal tides is based on comparison of AOTIM-derived M_2 and S_2 constituents and semi-diurnal band-passed depth-averaged ADCP data (see section 4.2). Averages are given within the pycnocline, and from a 30-m interval below the pycnocline: ε is the dissipation, N is the buoyancy frequency, K_ρ is the eddy diffusivity, and KE is the kinetic energy per unit mass. For ε, N and K_ρ, standard deviation values for the sets of each station are given in parenthesis.

Station	**X**	**XI**	**XIII**	**XIV**	**XVI**	**XVII**
D_{mixed} [m]	-	7	8	21	9	24
D_{pyc} [m]	26	29	39	37	56	40
E_{10} [W m^{-2}]	0.50	2.53	0.54	6.42	4.48	2.19
Var explained by semi-diurnal tides (%)	46	89	see text	2	63	70
Averages over $D_{mixed}<z<D_{pyc}$						
ε [10^{-7} W kg^{-1}]	0.30 (0.17)	10.4 (5.4)	17.3 (21.4)	6.0 (7.3)	4.7 (6.8)	1.1 (1.5)
N [10^{-3} s^{-1}]	19.0 (0.9)	17.3 (3.2)	15.9 (2.5)	7.8 (1.6)	8.4 (1.0)	7.4 (1.7)
$K\rho$ [10^{-4} m^2 s^{-1}]	0.09 (0.02)	6.8 (9.8)	9.4 (8.9)	44.6 (72)	15.1 (22.9)	6.1 (11.6)
KE [10^{-2} J kg^{-1}]	1.0	3.1	22.1	2.4	3.1	0.8
Averages over $D_{pyc}<z<D_{pyc}+30$						
ε [10^{-7} W kg^{-1}]	0.12 (0.01)	0.88 (1.0)	2.8 (0.7)	0.21 (0.03)	0.23 (0.01)	0.25 (0.04)
N [10^{-3} s^{-1}]	6.9 (0.6)	6.5 (0.6)	7.6 (2.6)	6.0 (1.2)	4.9 (0.6)	3.4 (0.9)
$K\rho$ [10^{-4} m^2 s^{-1}]	0.36 (0.05)	2.8 (3.2)	14.4 (13.8)	1.1 (0.5)	1.5 (0.6)	4.7 (3.7)
KE [10^{-2} J kg^{-1}]	1.3	2.8	12.6	2.5	2.2	0.8

Table 3. Station mean results from internal-wave mixing models for dissipation. N is observed buoyancy frequency, N_0 = 3 cph is the reference buoyancy frequency, Sh^2 is the observed shear variance, and Sh^2_{GM} is the shear variance from the Garrett-Munk model. ε is measured dissipation for the depth intervals where models were applied and subscripts for the different models are G89 for *Gregg* [1989], GH for Gregg-Henyey [*Gregg*, 1989] and MG for *MacKinnon-Gregg* [2003a]. CW/CCW indicates the ratio of the clockwise to counterclockwise velocity variance evaluated at the lowest resolved wavenumber of the vertical wavenumber spectrum. CW/CCW>1 indicates downward propagating low-mode internal wave energy.

Station	**X**	**XI**	**XIII**	**XIV**	**XVI**	**XVII**
N^2/N_0^2	1.8	1.8	3.2	0.8	1.0	0.6
Sh^2/Sh^2_{GM}	0.3	2.3	5.3	2.0	1.1	0.7
ε [10^{-7} W kg^{-1}]	0.23	1.12	2.25	0.59	0.32	0.33
$\varepsilon/\varepsilon_{G89}$	191.5	17.5	3.6	28.0	38.7	174.8
$\varepsilon/\varepsilon_{GH}$	128	11.7	2.4	18.7	25.9	116.8
$\varepsilon/\varepsilon_{MG}$	0.8	1.4	1.0	1.8	1.0	2.3
CW/CCW	4.3	0.1	0.3	1.1	4.7	0.4

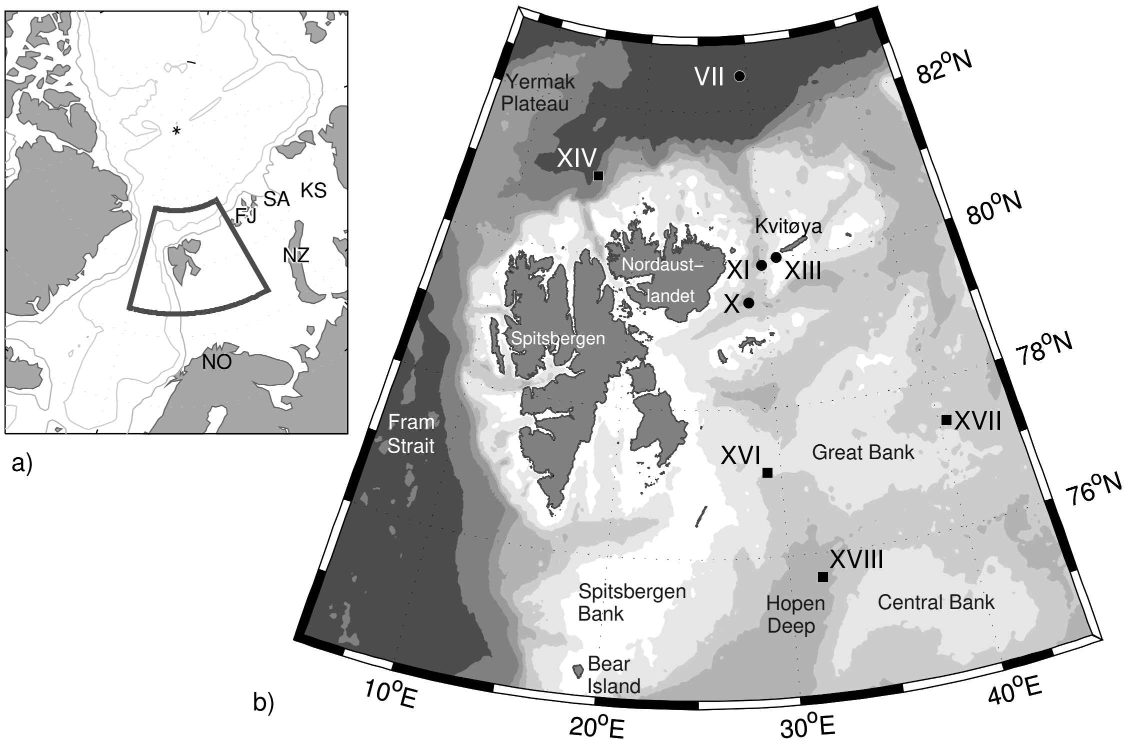

Figure 1. a) Map showing the location of the study area and b) a blow-up with mean positions of the ice drift stations (2004 – bullets, 2005 – squares). Isobaths are gray-shaded at 100, 200, 300, 500, 1000 and 2000 m. Abbreviations in a) mark the locations of St. Anna Trough (SA), the Kara Sea (KS), Novaya Zemlya (NZ), Franz Josef Land (FJ) and the coast of Norway (NO).

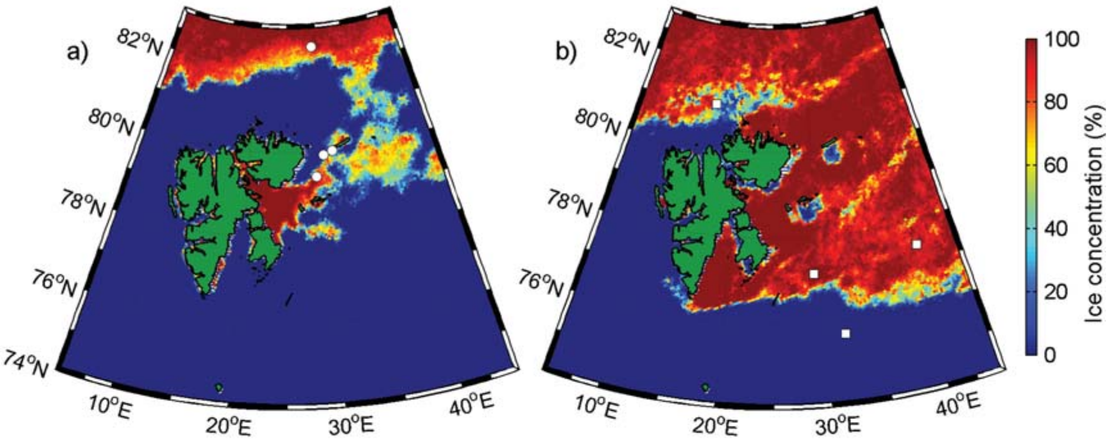

Figure 2. Ice concentrations at the beginning of each cruise: a) 20 July 2004, and b) 19 May 2005. Station positions are indicated with white bullets and squares. See Figure 1b for station names. Satellite-derived data are obtained from http://iup.physik.uni-bremen.de:8084/amsr/amsre.html.

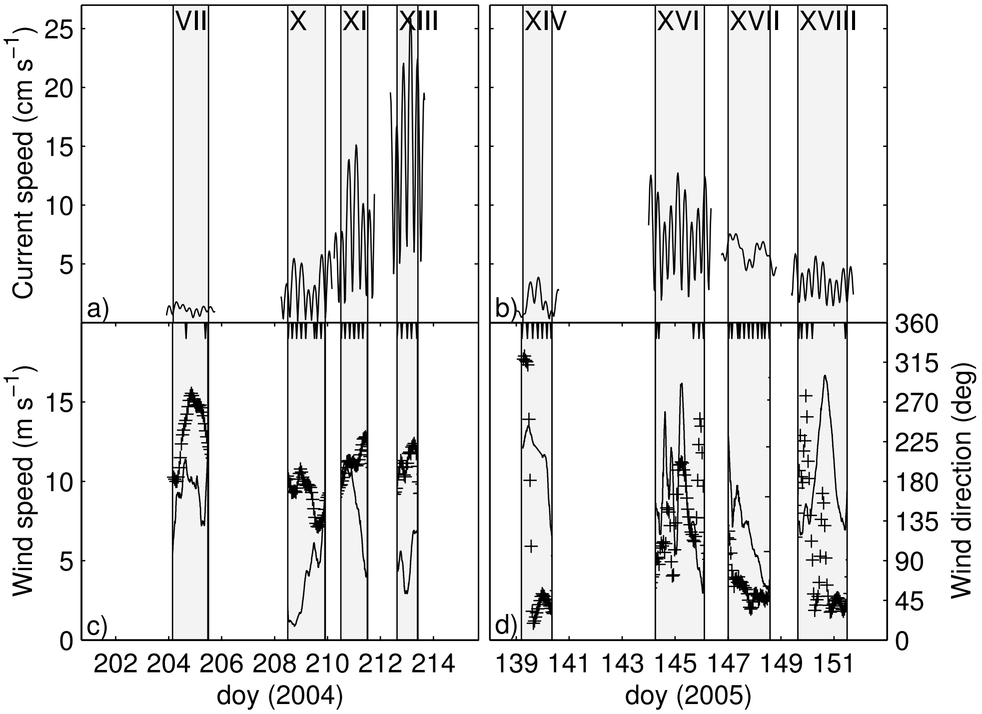

Figure 3. Upper panels: tidal current speeds from AOTIM predicted at the mean position of each station for a) 2004 and b) 2005. Duration of each station is shaded, with names indicated. Lower panels: wind speed (line) and direction (crosses) for c) 2004 and d) 2005. Start time of the MSS sets are marked by arrowheads on top.

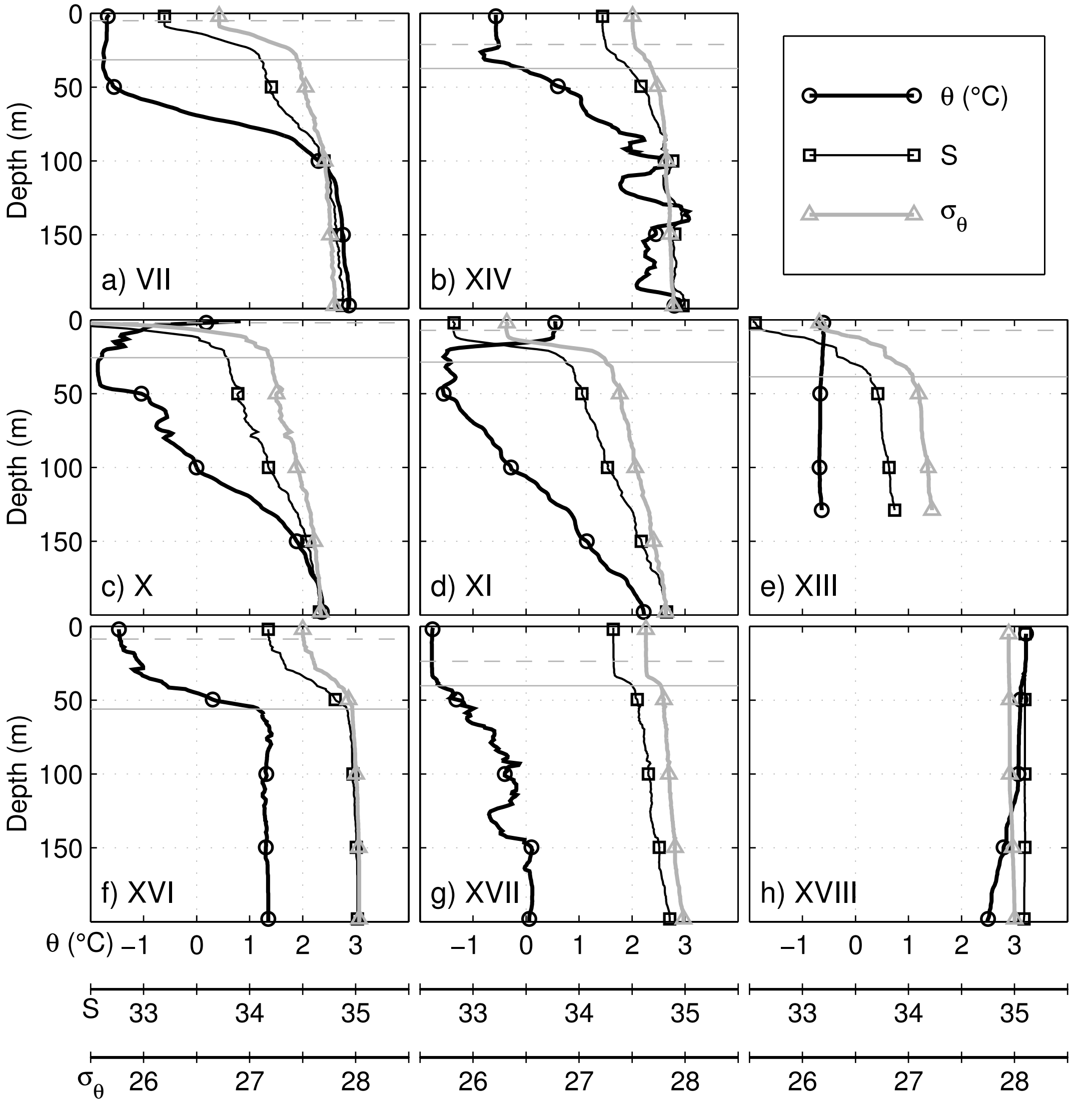

Figure 4. Representative CTD profiles from the Northern shelf slope stations a) VII and b) XIV, the Interior MIZ stations c) X, d) XI and e) XIII, and the Southern MIZ stations f) XVI, g) XVII and h) XVIII. Station-mean depths of the surface mixed layer, D_{mixed}, (dashed gray lines) and the base of the pycnocline, D_{pyc}, (solid gray lines) are indicated.

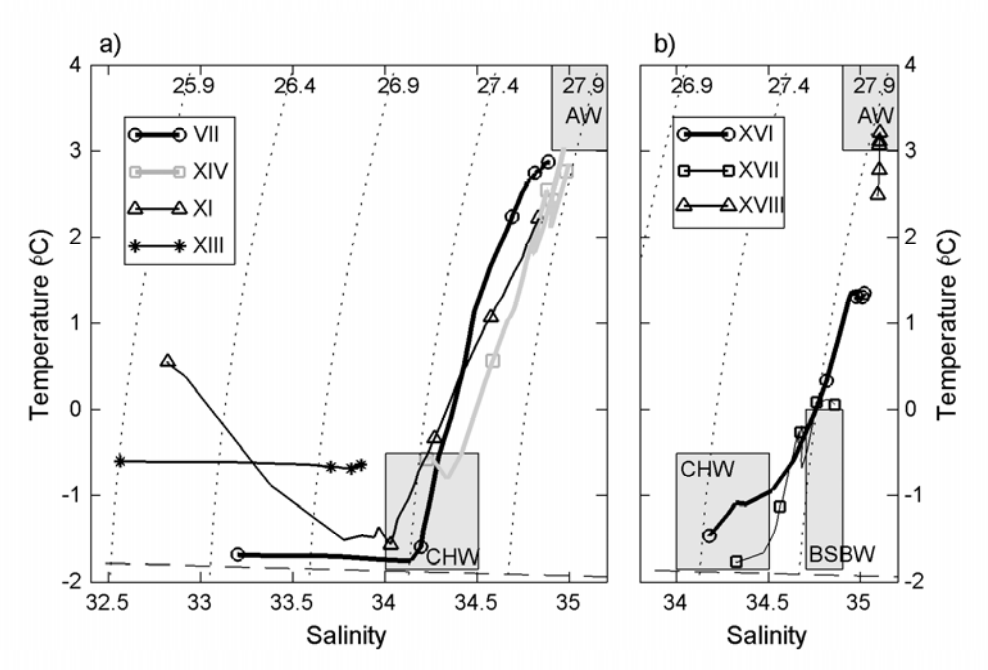

Figure 5. Temperature-salinity plots from a) the Northern and Interior stations and b) the Southern MIZ stations. Shaded boxes denote the Atlantic Water (AW), the Cold Halocline Water (CHW) and the Barents Sea Branch Water (BSBW). Markers are placed at 50-m intervals from surface to a common maximum depth of 200 m, except for XIII which was ~150 m at the deepest. T-S values are bin-averaged over 5-m intervals for clarity. Dotted contours are σ_θ isolines and the dashed line is the freezing temperature.

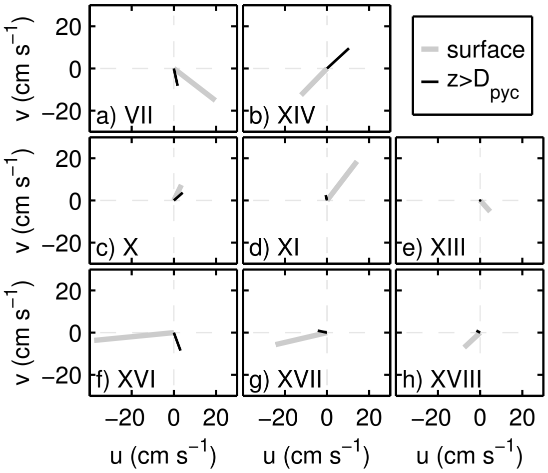

Figure 6. Average vectors of surface drift (gray) and depth-averaged current from below the pycnocline (black) at the Northern shelf slope a) VII and b) XIV, the Interior MIZ c) X, d) XI and e) XIII, and the Southern MIZ f) XVI, g) XVII and h) XVIII. Averaging is done over the first 24.8 h (2 M_2 cycles) of each station when station duration allows (22.6 h at VII, 20.1 h at XIII). Only the surface current is shown for XIII due to large depth variability during station time.

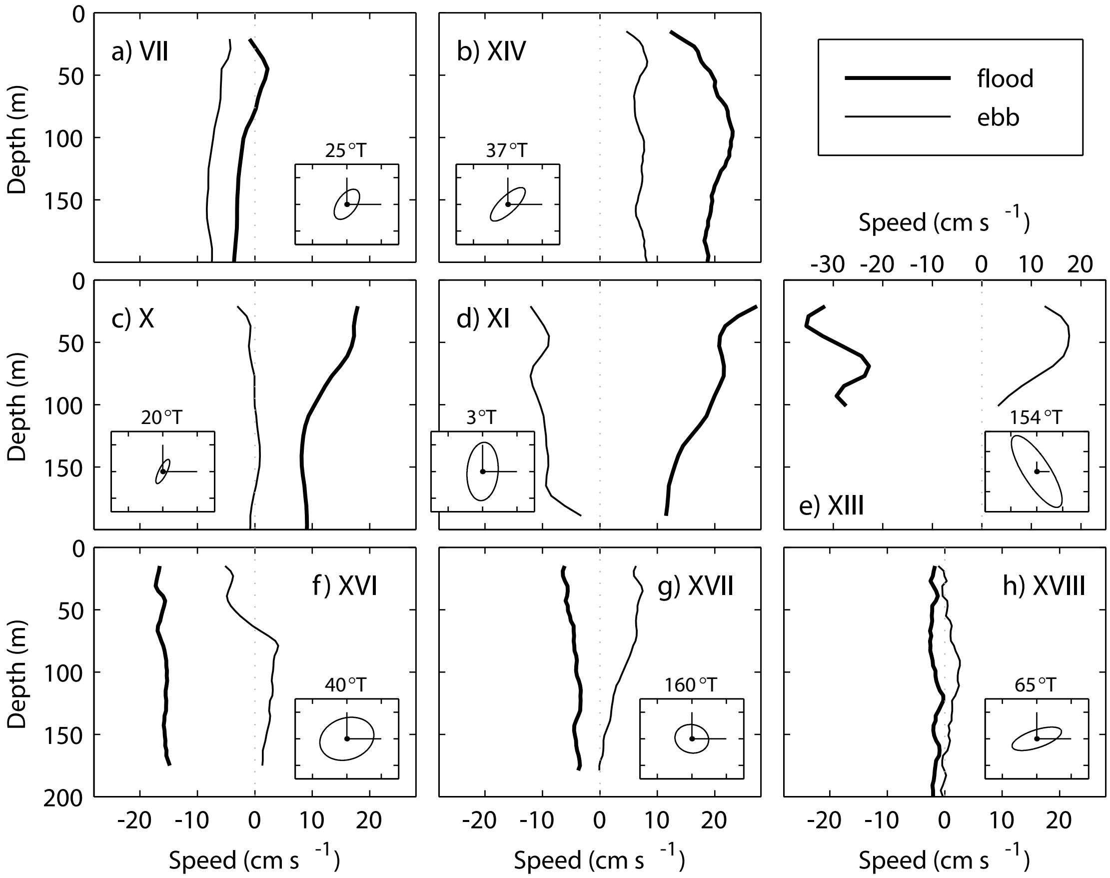

Figure 7. Ensemble averaged velocity profiles during times of flood (thick) and ebb (thin) along the principle axis of the depth-averaged current at the Northern shelf slope a) VII and b) XIV, the Interior MIZ c) X, d) XI and e) XIII, and the Southern MIZ f) XVI, g) XVII and h) XVIII. The ellipses of the depth-averaged current are shown as insets with the principle axis orientation indicated as degrees true. Orthogonal lines emanating from the origin are 10 cm s^{-1}, shown for reference. Note that the horizontal scale is different in e).

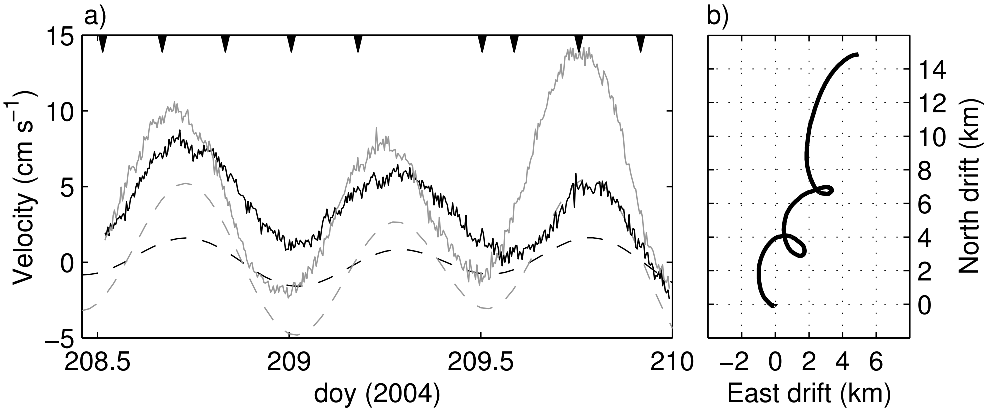

Figure 8. a) East (black) and north (gray) components of the depth-averaged ADCP velocity (solid lines) at station X compared with AOTIM-derived tidal velocity (dashed). Arrowheads on top show start times of the MSS sets. b) Surface drift path at X.

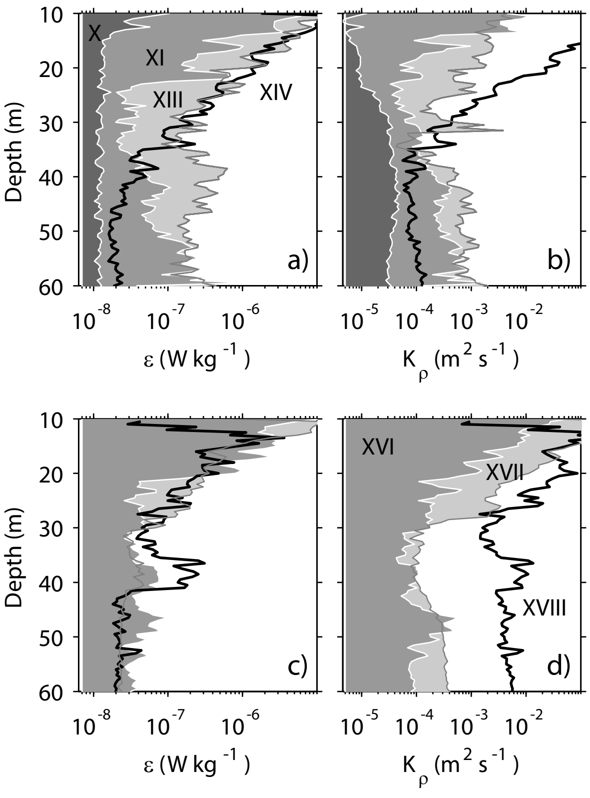

Figure 9. Profiles of the station-mean dissipation, ε, from shear measurements (left panels, a), c)) and the corresponding eddy diffusivity, K_ρ (right panels, b), d)) in the upper 60 m for the Northern and Interior stations (upper panels) and the Southern MIZ stations (lower panels).

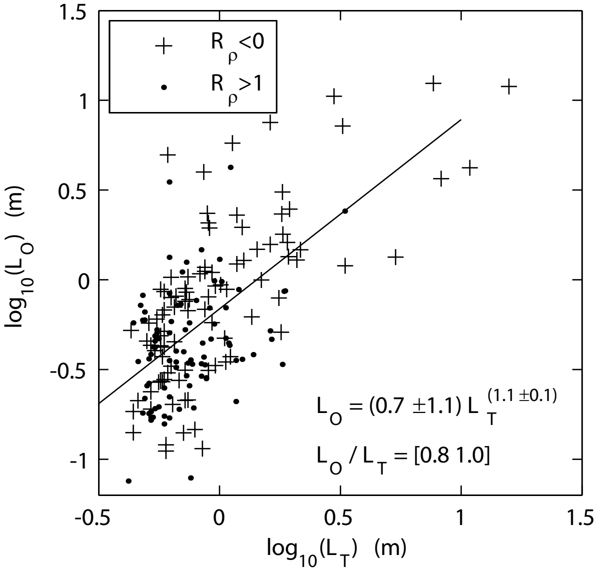

Figure 10. Log-log scatter plot of the Thorpe scale, L_T, versus the Ozmidov scale, L_O. Data points from when the background stratification was stable to DDC (crosses) and diffusive layer favorable (dots) are shown separately. The equation resulting from the least-squares regression is indicated with ± standard error. The 95 % confidence levels of the maximum likelihood estimator from a log-normal distribution of the L_O/L_T ratio is [0.8 1.0].

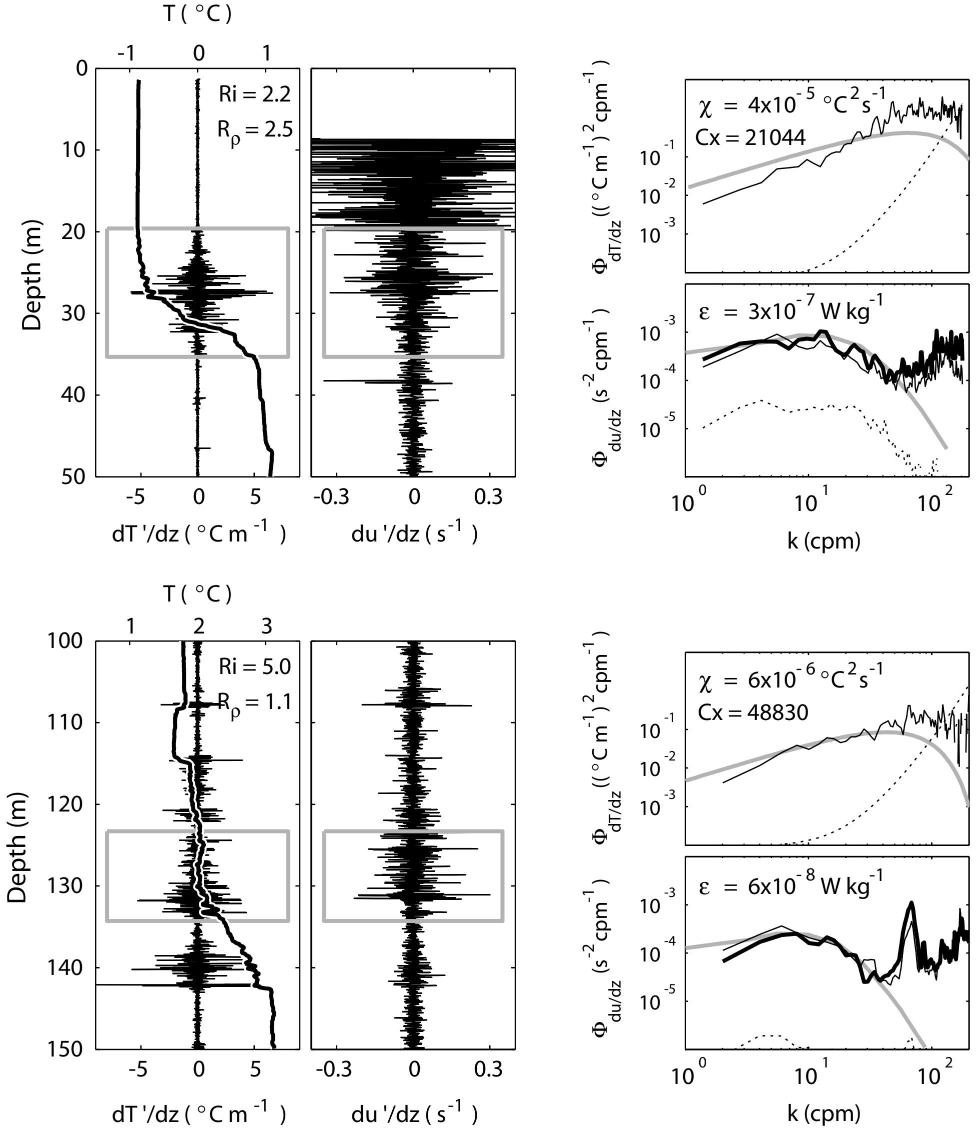

Figure 11. Two examples of patches of enhanced temperature gradient. The profiles are (left) temperature and 30 Hz low-passed temperature gradient, (middle) 10 Hz low-passed shear from one of the shear probes. The vertical extent of the patches are indicated by gray boxes. The temperature gradient spectra ($\Phi_{dT/dz}$) and shear spectra ($\Phi_{du/dz}$) calculated for each patch are shown at the last column. The corresponding gray traces are the Batchelor's and Nasmyth's form of the universal $\Phi_{dT/dz}$ and $\Phi_{du/dz}$ spectra, respectively. Shear spectra from both shear probes are shown (thin and thick traces). The dashed shear spectrum is that inferred from the acceleration sensor of the instrument

(acceleration spectrum divided by the sinking speed squared) and is indicative of the noise induced by the instrument's motion. The dashed dT/dz spectra are the noise level inferred from quiescent portions of the temperature gradient record. The mean values of the Richardson number, Ri, the density ratio, R_ρ, the dissipation of temperature variance, χ, the Cox number, Cx, and the dissipation of TKE, ε, are indicated for each patch. Both patches are recorded at station XIV.

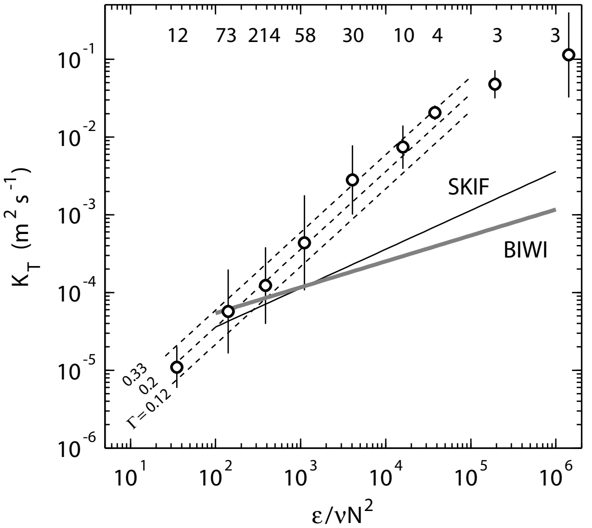

Figure 12. Variation of the diffusivity for heat, K_T, with the buoyancy Reynolds number, $\varepsilon/\nu N^2$ estimated for detected turbulent temperature patches (407 in total). The values of K_T are averaged in equally spaced logarithmic bins of $\varepsilon/\nu N^2$. Error bars indicate ± 1 standard deviation over the number of data points indicated at top. The models shown are that of Osborn using Γ=0.12, 0.2, and 0.33 (dashed), SKIF (thin black) and BIWI (thick gray).

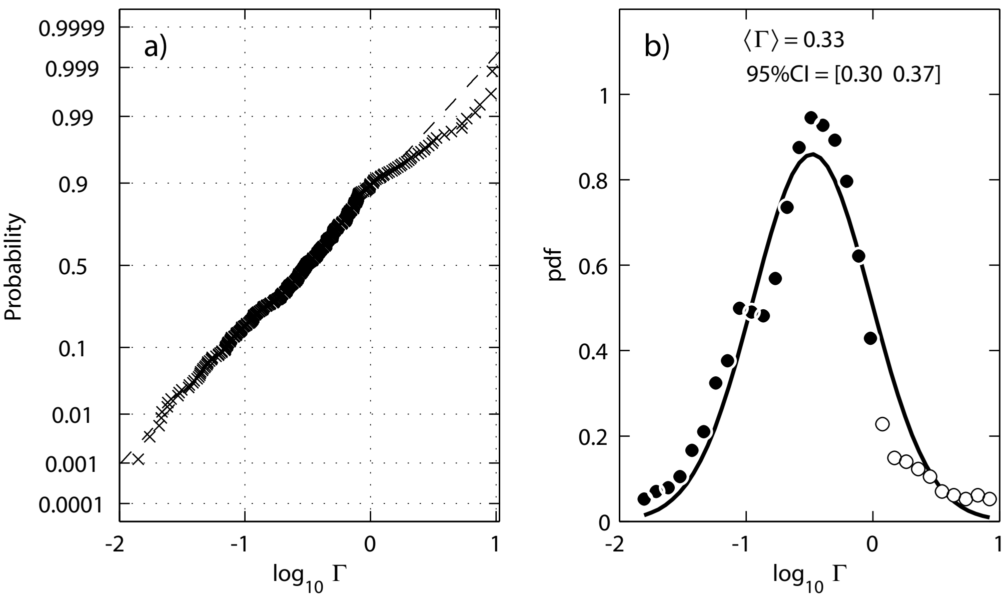

Figure 13. a) Normal probability plot for $\log_{10}\Gamma$. b) Probability density derived from the histogram of $\log_{10}\Gamma$ (filled and open circles) and the normal probability density function (black curve) fitted (non-linear least squares fit) to the values of $\Gamma < 1$ (filled circles). The expected mean value and 95% confidence intervals for the fitted distribution are indicated.

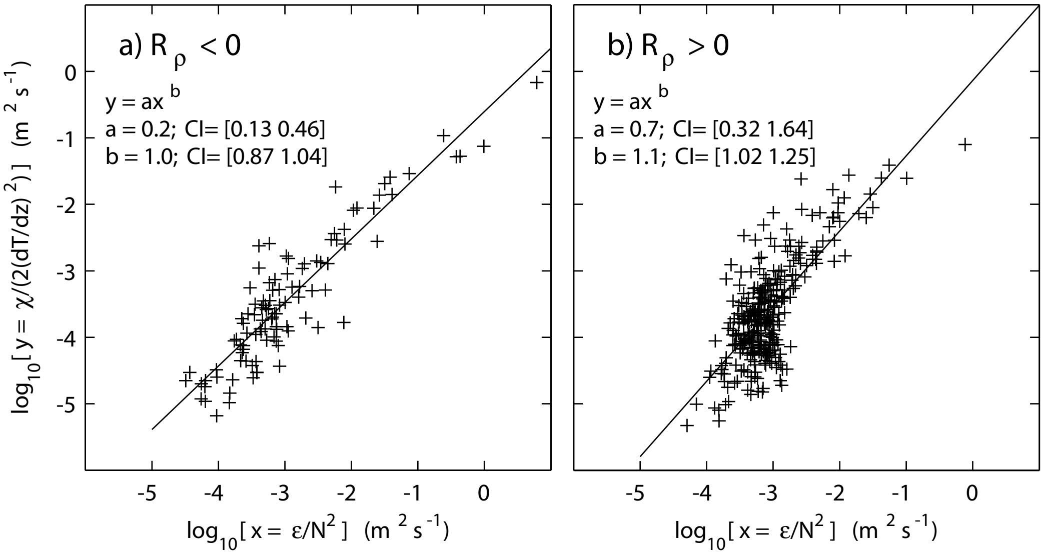

Figure 14. Regression of $x = \varepsilon/N^2$ on $y = \chi/[2(dT/dz)^2]$ on log-log space for a) diffusively stable patches (102 data points) and b) double diffusion favorable patches (305 data points). The best-fit values of a and b and their 95% confidence intervals are indicated.

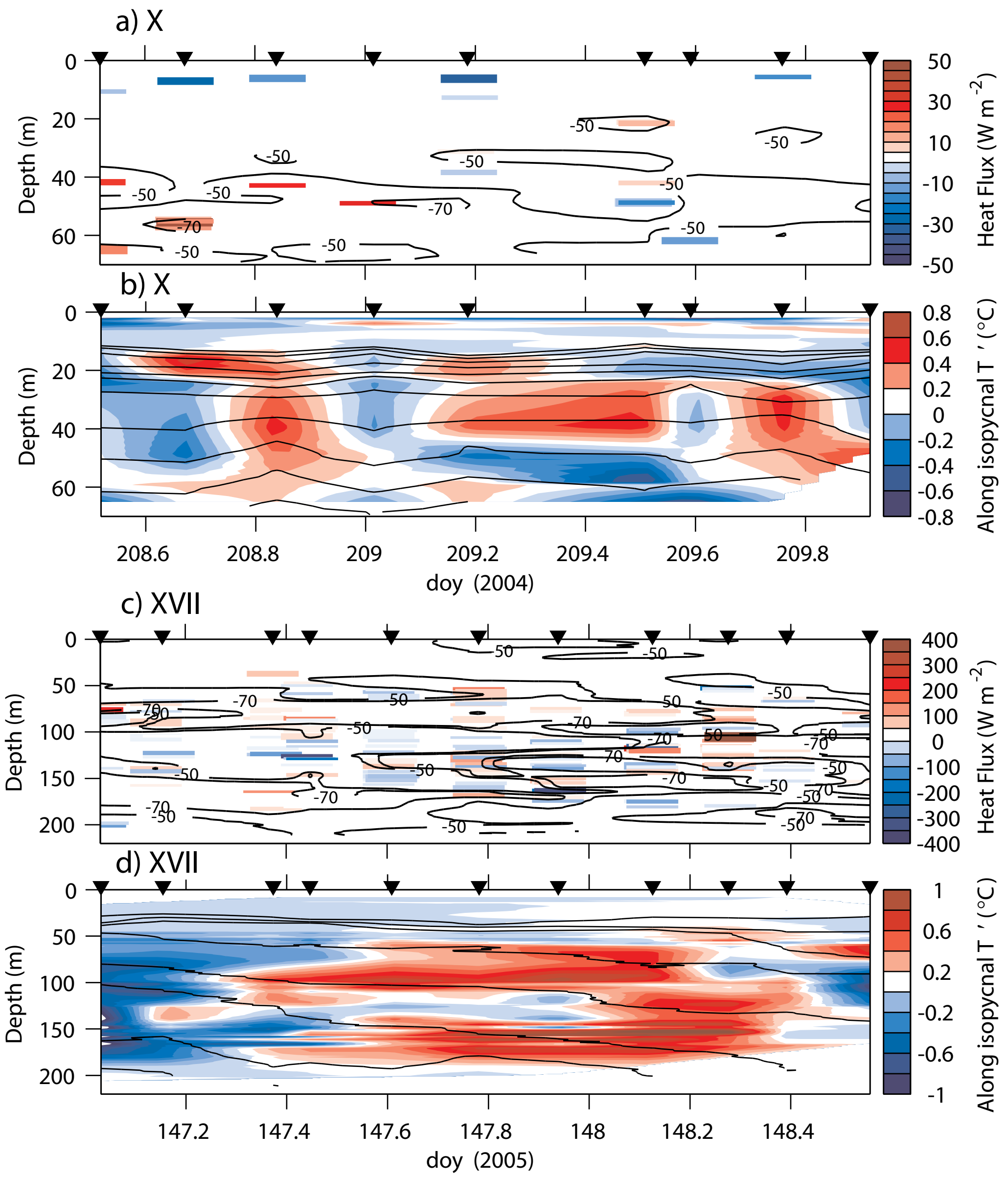

Figure 15. Depth versus time maps of heat flux (boxes in color) and Turner angle (black isolines) at a) X and c) XVII, and of temperature anomaly along mean isopycnals at b) X and d) XVII. Isopycnals, $\sigma_\theta>27$, are contoured at 0.05 intervals in b) and d). Heat fluxes from Osborn-Cox method are shown for all available patches (23 at X, and 192 at XVII). The vertical extent of each box show the position of the patch in the water column where as the horizontal extent is arbitrary.

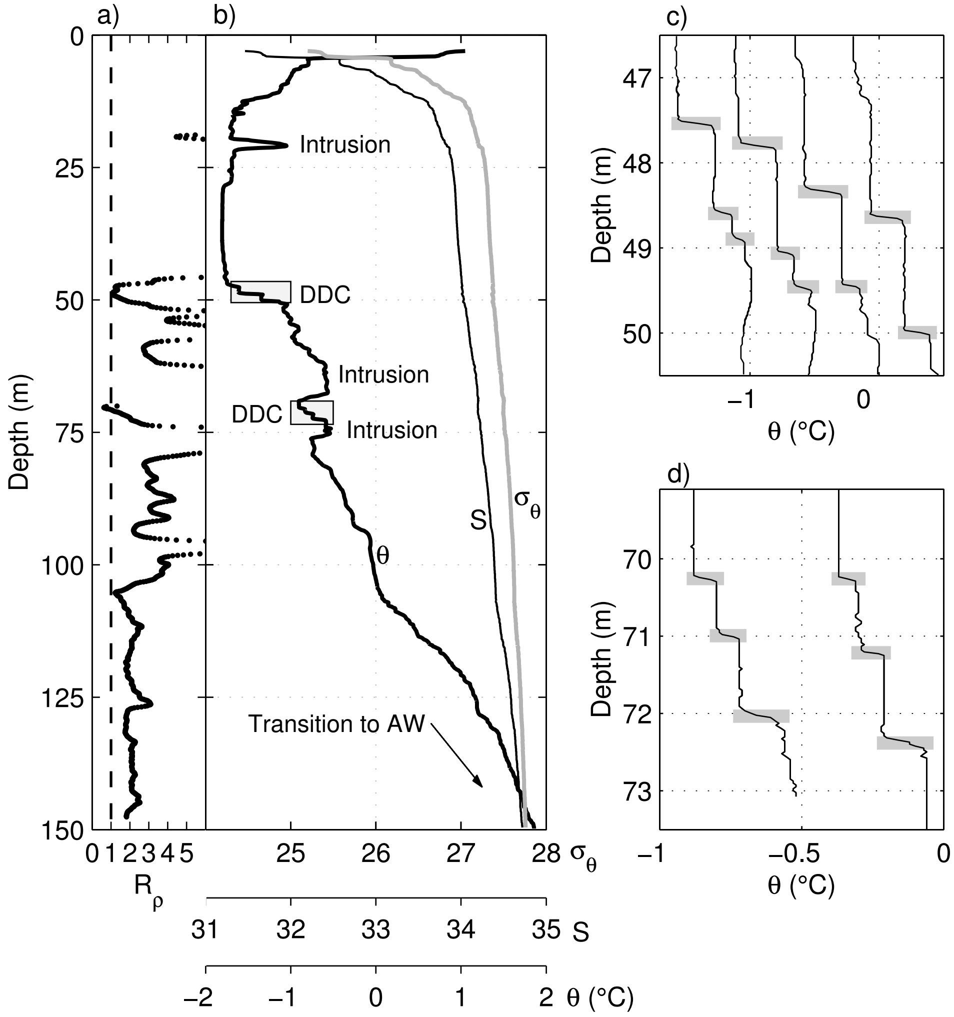

Figure 16. a) Density ratio, R$_\rho$ and b) temperature (thick black), salinity (thin black), and σ_θ (gray) profiles at station X. Two selected regions with double diffusive convection (DDC) steps, indicated by boxes in b), are expanded in panels on the right for c) the upper DDC box (along with three preceding profiles, offset by 0.5 °C) and d) the deeper box (along with one preceding profile). Interfaces of DDC steps that passed the criteria (section 3.5) are marked with thick gray lines in c-d. Note how the main structure is maintained between deployments but shifted in depth in both c) and d).

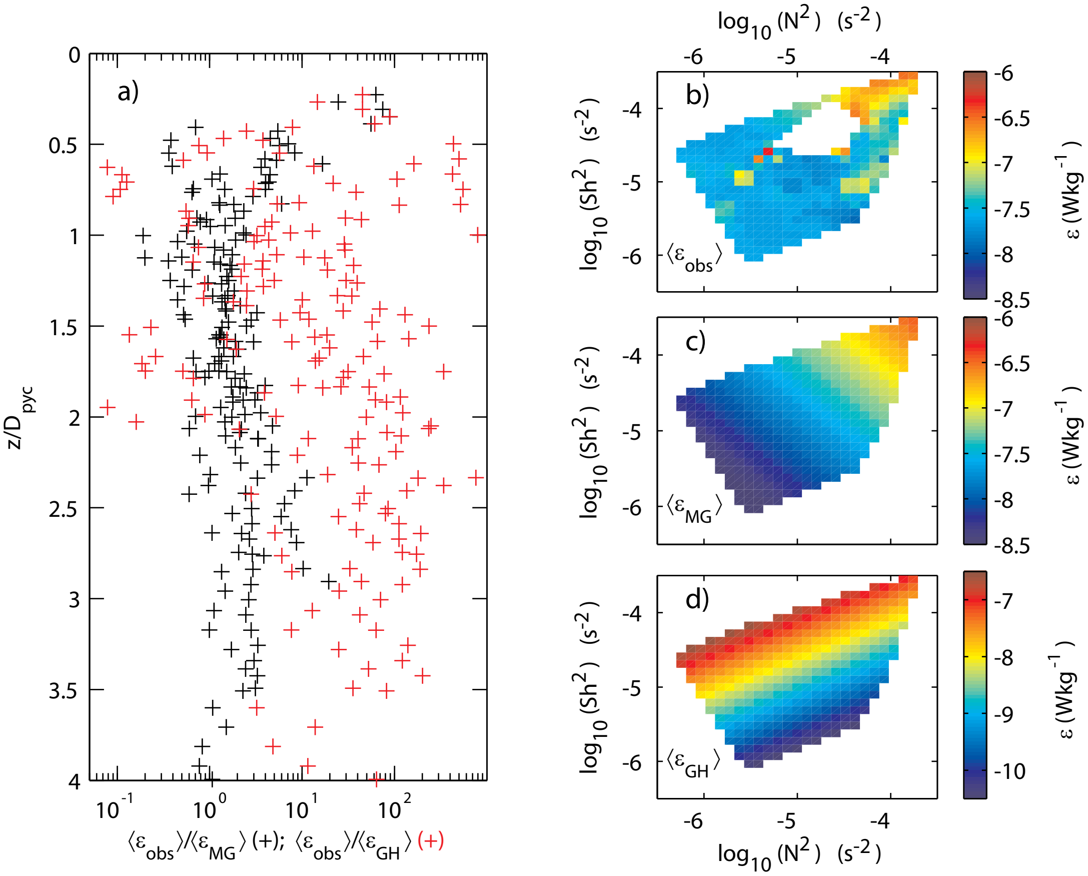

Figure 17. a) Profiles of the ratio of the observed dissipation, ε_{obs}, to that derived from Gregg-Henyey model ε_{GH} (red, Eq. 3) and MacKinnon and Gregg model, ε_{MG} (black, Eq. 4). Ordinate is depth scaled with the base of the pycnocline. Distribution of b) ε_{obs} , c) ε_{MG} and d) ε_{GH} in log-log $N^2 - Sh^2$ space. Note the different color scale in d).